Editing of endogenous tubulins reveals varying effects of tubulin posttranslational modifications on axonal growth and regeneration

Yu-Ming Lu[1], Shan Yan[2], Shih-Chieh Ti[2], and Chaogu Zheng[1,*]

[1]School of Biological Sciences, Faculty of Science, The University of Hong Kong, Hong Kong SAR, China

[2]School of Biomedical Sciences, Li Ka Shing Faculty of Medicine, The University of Hong Kong, Hong Kong SAR, China.

[*]Correspondence: cgzheng@hku.hk (C.Z.)

Abstract

Tubulin posttranslational modifications (PTMs) modulate the dynamic properties of microtubules and their interactions with other proteins. However, the effects of tubulin PTMs were often revealed indirectly through the deletion of modifying enzymes or the overexpression of tubulin mutants. In this study, we directly edited the endogenous tubulin loci to install PTM-mimicking or -disabling mutations and studied their effects on microtubule stability, neurite outgrowth, axonal regeneration, cargo transport, and sensory functions in the touch receptor neurons of *Caenorhabditis elegans*. We found that the status of β-tubulin S172 phosphorylation and K252 acetylation strongly affected microtubule dynamics, neurite growth, and regeneration, whereas α-tubulin K40 acetylation had little influence. Polyglutamylation and detyrosination in the tubulin C-terminal tail had more subtle effects on microtubule stability likely by modulating the interaction with kinesin-13. Overall, our study systematically assessed and compared several tubulin PTMs for their impacts on neuronal differentiation and regeneration and established an *in vivo* platform to test the function of tubulin PTMs in neurons.

Introduction

Microtubules (MTs) play important roles in neuronal development by providing structural support for neurite growth and serving as tracks for intracellular transport. MTs are formed by the polymerization of α/β-tubulin heterodimers, which are crucial determinants of MT properties. Eukaryotic genomes contain multiple α- and β-tubulin genes (called isotypes) with distinct expression patterns and dynamic properties (Janke and Magiera, 2020; Lu and Zheng, 2022; Nsamba and Gupta, 2022). These tubulin isotypes are also subjected to a range of post-translational modifications (PTMs), which regulate the stability of MTs and their interaction with various microtubule-associated proteins (MAPs) (Roll-Mecak, 2020). The findings of multiple tubulin isotypes with different PTMs led to the concept of "tubulin code", which suggests that the structure, dynamics, and functions of individual MTs are controlled by the tubulin isotype composition and the tubulin PTMs (Janke, 2014). Perturbation to the tubulin code can lead to MT dysfunction and are linked to human diseases (Tischfield et al., 2011).

Although previous research described the effects of several tubulin PTMs in neuronal development, these earlier studies have two potential limitations. First, the role of tubulin PTMs was often revealed by the overexpression of tubulin mutants with PTM-mimicking or unmodifiable amino acid substitutions (Shida et al., 2010). Such overexpression may create artifacts. Moreover, since the tubulin concentration in cells is controlled by autoregulation through mRNA degradation (Lin et al., 2020), overexpression of exogenous tubulins may trigger the downregulation of endogenous tubulin isotypes, complicating the interpretation of the results. Second, the effects of tubulin PTMs were also identified by studying the enzymes that add or remove specific PTMs. In some cases, the phenotypes caused by deleting the enzyme may not be the same as the elimination of the tubulin PTMs, because the enzyme may have multiple substrates, including non-tubulin substrates, or the enzyme has additional functions independent of its activity in modifying tubulins. For example, the function of α-tubulin acetyltransferase MEC-17 in regulating neurite outgrowth is independent of its enzymatic activities (Topalidou et al., 2012). Given the above two limitations and recent advance in genome editing, we reason that the role of tubulin PTMs can be directly assessed by engineering the endogenous tubulin genes.

In this study, we installed PTM-mimicking or -inactivating mutations in the endogenous loci of the *Caenorhabditis elegans* tubulin genes that are specific for the touch receptor neurons (TRNs) and examined the effects of these mutations on neuronal development. We and others

63 previously established *C. elegans* TRNs as a model to study the effects of tubulin missense
64 mutations on MT stability and neurite growth at the single-cell level (Lee et al., 2021; Savage et
65 al., 1994; Zheng et al., 2017). TRNs are a set of six mechanosensory neurons that detect gentle
66 body touch and have long sensory neurites along the body wall. These neurites are filled with
67 specialized 15-protofilament MTs (Chalfie and Thomson, 1982), presumably made of MEC-
68 12/α-tubulin and MEC-7/β-tubulin, which are the dominant tubulin isotypes in the TRNs and are
69 expressed at much (>100 times) higher levels than other tubulin isotypes (Taylor et al., 2021).
70 Mutations in *mec-12* and *mec-7* led to the reduction of MT numbers, loss of the 15-protofilament
71 MT structure, alteration of MT stability, and defects in neurite growth and sensory functions in
72 the TRNs (Zheng et al., 2017), suggesting that MEC-12 and MEC-7 control MT structure and
73 function in the TRNs.
74 Moreover, through the analysis of ~100 missense mutations in *mec-12* and *mec-7*, our
75 previous work established three phenotypic categories for tubulin mutations: loss-of-function
76 (*lf*), which caused mild defects in neurite extension, antimorphic (*anti*), which led to significant
77 reduction in MT stability and caused strong defects in neurite growth, and neomorphic (*neo*)
78 alleles, which resulted in hyperstable MTs and excessive neurite growth (Lee et al., 2021; Zheng
79 et al., 2017). These distinct impacts of tubulin mutations on MT properties and neurite growth
80 patterns provide a framework to assess and compare the varying roles of different tubulin PTMs
81 in neuronal differentiation.
82 Here, by editing the endogenous *mec-12* and *mec-7* loci, we systematically studied the
83 effects of β-tubulin S172 phosphorylation and K252 acetylation, α-tubulin K40 acetylation, and
84 tubulin polyglutamylation and detyrosination on neurite growth and regeneration, MT stability,
85 cargo transport, and neuronal functions. We found that the status of β-tubulin S172
86 phosphorylation strongly affects MT dynamics and neurite development, whereas α-tubulin K40
87 acetylation did not appear to affect either neuronal morphology or function in any significant
88 way. Polyglutamylation and detyrosination of the tubulin C-terminal tail had more subtle effects
89 on regulating MT stability and limiting ectopic neurite growth likely by modulating the
90 interaction of microtubules with kinesin-13. Tubulin PTMs can have either negative or positive
91 effects on axonal regeneration depending on the type of modifications. Overall, our studies
92 establish a platform to analyze the effects of tubulin PTMs on neuronal differentiation and
93 regeneration through the editing of neuron type-specific tubulin isotypes.

Results

β-tubulin S172 phosphorylation inhibits neurite growth

The first PTM we analyzed was the phosphorylation of β-tubulin at the well-conserved serine 172 (S172) residue (Figure 1-figure supplement 1A). In mitotic cells, S172 phosphorylation by cyclin-dependent kinase Cdk1 led to the exclusion of the tubulins from the MTs likely because S172 phosphorylation interfered with both GTP binding to β-tubulin and the longitudinal interdimer interaction (Fourest-Lieuvin et al., 2006). In neurons, Ori-McKenney et al. (2016) found that the Minibrain Kinase (MNB) regulated MT dynamics and dendritic morphogenesis of the Drosophila class III da neurons, and Drosophila MNB was able to phosphorylate porcine β-tubulin at S172 *in vitro*. These results suggested that β-tubulin S172 phosphorylation may be a regulatory point for MT stability in neurons. However, the role of S172 in neurite growth has not been tested directly.

We created the phospho-mimicking S172E and the nonphosphorylatable S172A mutations in the endogenous *mec-7* locus through CRISPR/Cas9-mediated gene editing. We found that the *mec-7(S172E)* mutation led to severe defects in axonal growth in TRNs, since all neurites of ALM and PLM neurons, the two major TRN subtypes, were significantly shortened in *mec-7(S172E)* mutant animals. The two anteriorly directed neurites of ALM and PLM were termed ALM-AN and PLM-AN; the posteriorly directed neurite of PLM was termed PLM-PN (Figure 1A-G). The phenotypes of S172E mutation were similar to our previously characterized *mec-7(anti)* alleles, which strongly suppressed neurite growth by blocking MT polymerization. In contrast, we observed the growth of an ectopic ALM posterior neurite (ALM-PN) in animals carrying the *mec-7(S172A)* mutation; this phenotype was similar to the *mec-7(neo)* alleles, which induced the growth of the ectopic ALM-PN by increasing MT stability. *mec-7(S172A)* mutants showed mild shortening of ALM-AN and PLM-AN, which were also observed with other *mec-7(neo)* alleles (Zheng et al., 2017). Being consistent with the genetic nature of gain-of-function mutants, both S172E and S172A mutations were semidominant as heterozygotes showed similar but less severe phenotypes than the homozygotes (Figure 1-figure supplement 1B-C).

Moreover, the *mec-7(S172P)* mutants, which we created to mimic a human TUBB2B missense mutation found in patients with cortical malformations (Jaglin et al., 2009), showed a *lf* phenotype with moderate defects in neurite growth (Figure 1A). Thus, S172E, S172A, and S172P mutations had three distinct phenotypes matching the three categories we previously

125 defined (Zheng et al., 2017). Based on these phenotypic similarities, we reasoned that increased
126 phosphorylation (S172E) likely prevented polymerization, leading to severe defects in neurite
127 extension, whereas abolishing phosphorylation (S172A) led to hyperstable MTs and excessive
128 neurite growth. The S172P mutation probably disrupted protein folding or blocked GTP binding,
129 which rendered MEC-7 inactive and caused a *lf* phenotype identical to the *mec-7(-)* mutants
130 (Zheng et al., 2017).
131 To confirm that MEC-7 S172 phosphorylation affects neurite growth cell-autonomously,
132 we extracted the TRNs from the embryos and differentiated them *in vitro*. Wild-type TRNs grew
133 long neurites in culture, whereas S172E but not S172A mutation significantly shortened the *in*
134 *vitro* developed neurites, supporting that S172 phosphorylation controls neuronal morphology in
135 a cell-intrinsic manner (Figure 1H-I). We also stained these *in vitro* cultured TRNs with anti-
136 phospho-tubulin (S172) antibodies and found a considerable reduction of the staining signal in
137 S172A mutant TRNs (Figure 1-figure supplement 2). We assumed the residual signal came from
138 other phosphorylated β-tubulin isotypes expressed in the cells or nonspecific binding of the
139 antibody.
140
141 **β-tubulin S172 phosphorylation reduces MT stability**
142 Next, we examined MT dynamics by tracking the plus-end binding protein EBP-2. We
143 found that the wild-type TRNs showed only a few EBP-2 comets due to very stable MTs as
144 previously reported (Lee et al., 2021), whereas S172E mutants had increased number of EBP-2
145 tracks, suggesting increased MT dynamics (Figure 2A-B). Moreover, anterior neurites in wild-
146 type TRNs (e.g., ALM-AN) had uniformly plus-end-out MTs, whereas S172E mutants showed
147 mixed MT polarity (Figure 2C). The altered MT dynamic properties were consistent with the
148 defects in neurite growth. To assess the difference in MT stability between the wild-type and
149 S172A mutants (both of which showed limited dynamics under normal conditions), we treated
150 the animals with low concentration of colchicine to depolymerize the MTs and then monitored
151 MT dynamics during the recovery phase. Under this sensitized condition, we found that S172A
152 mutants showed fewer EBP-2 comets than the wild-type animals, which suggested reduced MT
153 dynamics and elevated stability (Figure 2A-B). Nevertheless, MT polarity was preserved in *mec-*
154 *7(S172A*) mutants (Figure 2C). These results supported that β-tubulin S172 phosphorylation
155 promotes dynamic MTs, which negatively regulates neurite growth.

156 In addition, the EBP-2::GFP signal in the cell body showed an unusual fiber-like shape in
157 the *mec-7(S172A)* mutants instead of the diffusive pattern in the wild-type (Figure 2D),
158 indicating the possible existence of MT bundles in the *S172A* cell body. In the wild-type TRNs,
159 the MT bundles were only found in the axons but not the cell body according to previous
160 electron microscopy studies (Chalfie and Thomson, 1979). Another hypothesis is that the
161 incorporation of nonphosphorylatable MEC-7(S172A) into MTs might affect GTP hydrolysis
162 and thus expand the EBP-2 binding region beyond the MT tips, since EB2 has a specific
163 nucleotide-dependent binding property (Roth et al., 2018).
164 S172 phosphorylation also affected cargo transport in TRNs. Mitochondrial transport was
165 impaired in *mec-7(S172E)* mutants, resulting in lower density of mitochondria along the axons
166 (Figure 2E-F). In contrast, *mec-7(S172A)* mutants showed higher accumulation of mitochondria
167 in the distal segment of the ALM-AN than the wild type. Moreover, the transport of synaptic
168 vesicles was also disrupted in *mec-7(S172E)* mutants. For example, wild-type PLM-AN branches
169 at a position close to the vulva; the branch forms chemical synapses with the neurites in the
170 ventral nerve cord, where the synaptic vesicles are transported to (Figure 2G). In *mec-7(S172E)*
171 mutants, the vesicles were mostly trapped in the cell bodies or along the proximal segment of the
172 neurite, probably due to highly unstable MTs (Figure 2G). About 40% of PLM-AN in *mec-*
173 *7(S172A)* mutants grew no branches or had a "hook" defect, and in these cases synaptic vesicles
174 were trapped at the distal end of the neurite (Figure 2G). Interestingly, synaptic vesicles were
175 also transported to the ectopic ALM-PN in *mec-7(S172A)* mutants (Figure 2G), as previously
176 observed in other *mec-7(neo)* mutants (Zheng et al., 2017).
177 At the behavioral level, both S172E and S172P mutants showed strong defects in touch
178 sensitivity, similar to the *mec-7(-)* deletion allele. The S172A mutants, however, did not reduce
179 touch sensitivity (Figure 2H). Since stable MTs are essential for the mechanosensory function of
180 the TRNs (Savage et al., 1989), reducing MT stability through S172 hyperphosphorylation was
181 expected to affect TRN functions.
182
183 **Optimal level of MEC-7/β-tubulin S172 phosphorylation is required for axonal**
184 **regeneration**
185 One of the important functions of MTs is to support neuronal regeneration, and previous
186 work have established the TRNs as an important model for axonal regeneration (Wu et al.,

187 2007). In our hands, following laser axotomy, ~72% wild-type PLM neurons were able to
188 regrow the proximal axon for a short length to connect with the distal fragment (defined as
189 reconnection), whereas the other ~28% PLM did not reconnect the severed axons and instead
190 grew the proximal axon for a substantial length (defined as regrowth). We found that the *mec-*
191 *7(S172E)* mutants were not able to reconnect the severed axons (only 4% reconnection) because
192 the regrowth length was very short (Figure 2I-K). A mesh-like structure with short sprouts were
193 observed at the regrowth site. We reasoned that the dynamic MTs may be too unstable to support
194 any substantial regrowth in the S172E mutants. Notably, these regeneration defects were
195 different from that seen in the *dlk-1(-)* mutants, which showed significantly reduced regrowth but
196 had no extensive sprouting (Figure 2I) probably due to the lack of MT polymerization at the
197 injury site (Ghosh-Roy et al., 2012).
198 The axonal regeneration in *mec-7(S172A)* mutants was also different from the wild-type.
199 Although 40% of the animals were able to reconnect the proximal axons with the distal segment,
200 the regrowth length was shorter than the wild-type animals (Figure 2I-J). Moreover, a highly
201 branched tree-like structure was seen at the regrowth site. It appears that the regrowth had no
202 clear direction. The regrowing axon extended multiple short processes towards different
203 directions, but none of these processes developed into a prominent axon. One possible
204 explanation is that the hyperstable MTs led to excessive neurite outgrowth and failure to properly
205 respond to guidance cues during regeneration. Interestingly, another *mec-7* neomorphic allele
206 that caused a P220S substitution also showed defects in axonal regeneration due to hyperstable
207 MTs (Kirszenblat et al., 2013). Thus, the above results suggested that an optimal level of β-
208 tubulin S172 phosphorylation is required for effective axonal regeneration.
209
210 **Enzymes mediating S172 phosphorylation in *C. elegans***
211 We next searched for the enzyme that mediates MEC-7 S172 phosphorylation by testing
212 the homologs of known kinases involved in phosphorylating β-tubulin. We first tested the two
213 close homologs of Minibrain kinase in *C. elegans*, *mbk-1* and *mbk-2*, both of which were
214 expressed in the TRNs based on fluorescent reporters (Figure 3-figure supplement 1A-B).
215 Mutations in *mbk-2* led to embryonic lethality and only a few animals could hatch and then arrest
216 at early larval stages (Quintin et al., 2003). We examined these arrested larvae but did not
217 observe excessive neurite growth as in S172A mutants. *mbk-1(-)* mutants were viable but did not

218 show any TRN developmental defects. We also examined the arrested larvae in *mbk-1(-) mbk-*
219 *2(-)* double mutants and could not observe the ectopic ALM-PN either (Figure 3-figure
220 supplement 1D). To knock down *mbk-2* expression in the TRNs specifically, we expressed
221 dsRNA against *mbk-2* from a TRN-specific *mec-17* promoter in both wild-type and *mbk-1(-)*
222 background and again failed to detect any changes in TRN morphology. We then attempted to
223 degrade the MBK-2 proteins specifically in the TRNs using a ZF1/ZIF-1 system (Wang et al.,
224 2017). We first edited the endogenous *mbk-2* locus to fuse GFP to an exon shared by all *mbk-2*
225 isoforms; to our surprise, we could not detect MBK-2::GFP signal in the TRNs although we
226 could observe the expected embryonic expression (Figure 3-figure supplement 2A-B). We
227 reasoned that the endogenous MBK-2 level might be very low in the TRNs. We then crossed
228 *mbk-2::gfp* into a strain expressing the GFP nanobody::ZIF-1 fusion specifically in the TRNs;
229 the resulted animals did not show long ALM-PN, suggesting that MBK-2, if expressed at low
230 level, was not likely to regulate TRN morphogenesis.
231 Minibrain kinase has a third, distant homolog in *C. elegans*, *hpk-1*, which is also the
232 homolog of human homeodomain-interacting protein kinase 1 (HIPK1). *hpk-1* was expressed in
233 the TRNs, but *hpk-1(-)* mutants did not show defects in TRN development (Figure 3-figure
234 supplement 1C-D). Based on the above results, we concluded that either high level of
235 redundancy existed among the Minibrain homologs or the Minibrain kinase was not the enzyme
236 catalyzing β-tubulin S172 phosphorylation in *C. elegans*.
237 Interestingly, the loss of the cyclin-dependent kinase Cdk1 led to the growth of ectopic
238 ALM-PN, similar to *mec-7(S172A)* mutants. We analyzed two deletion alleles (*he5* and *ok1882*)
239 of *cdk-1* (*C. elegans* Cdk1), both of which caused lethality. Maternally rescued homozygous *cdk-*
240 *1(-)* animals were arrested in early larval stages, but some escapers could reach late larval stages.
241 We found that the arrested *cdk-1(he5)* and *cdk-1(ok1882)* larvae grew an ectopic ALM-PN
242 (Figure 3A-B). Because these animals could not grow to the adult size, we measured the ALM-
243 PN/ALM-AN ratio and found that *cdk-1(-)* mutants had a similar ratio as the *mec-7(S172A)*
244 animals (Figure 3C). Moreover, the *cdk-1(-); mec-7(S172A)* double mutants showed the ALM-
245 PN length comparable to the two single mutants (Figure 3D), suggesting that they act in the same
246 pathway.
247 Finally, we tested the enzymatic activity of CDK1 towards the recombinant MEC-
248 12/MEC-7 α/β-tubulin heterodimer and found that CDK1 could indeed phosphorylate the S172

249 of MEC-7/β-tubulin (Figure 3E-F). In contrast, recombinant MBK-2 proteins did not show
250 kinase activities towards S172 of MEC-7 either in the same MEM reaction buffer (Figure 3E) or
251 in the BRB80 buffer (Figure 3-figure supplement 3) used by the previous studies of Drosophila
252 Minibrain (Ori-McKenney et al., 2016), which was consistent with the lack of ALM-PN
253 phenotype in *mbk-2(-)* mutants. Although *cdk-1/Cdk1* was known to be expressed mostly in
254 mitotic cells, some studies suggested a role for Cdk1 in postmitotic neurons (Kim and Bonni,
255 2008; Yuan et al., 2008), and cell cycle regulators (including cyclins) showed expression in
256 neurons (Akagawa et al., 2021). In fact, single-cell transcriptomic studies found weak expression
257 of cyclin A (*cya-1*) and cyclin B (*cyb-1*) in ALM neurons (Taylor et al., 2021). Thus, Cdk1 may
258 regulate neuronal differentiation by catalyzing β-tubulin S172 phosphorylation. Nevertheless, we
259 could not rule out the possibility that other kinases may also regulate S172 phosphorylation.
260

261 **MEC-12/α-tubulin K40 acetylation is not essential for TRN morphology and function**

262 α-tubulin acetylation, which occurred at the lysine 40 (K40) in the MT lumen, has been a
263 marker for stable MTs, particularly in neurons. Recent work found that K40 acetylation may
264 reduce lateral contact between protofilament, which increased the flexibility of MTs and
265 provided resistance to mechanical stress (Portran et al., 2017). In neurons, tubulin acetylation
266 promotes the transport of vesicles along the axons (Even et al., 2019). Altered tubulin acetylation
267 levels were often correlated with defects in neuronal morphogenesis (Chang et al., 2009), but
268 whether K40 acetylation has a direct impact on axonal growth is less clear.

269 Although K40 is quite conserved in α-tubulins across species, among the nine α-tubulin
270 isotypes in *C. elegans*, only MEC-12 has a K40 residue (Figure 4-figure supplement 1A). We
271 created acetyl-mimicking K40Q and unmodifiable K40R mutants through gene editing and
272 confirmed the change of tubulin acetylation status by observing the loss of anti-acetyl-α-tubulin
273 (K40) antibody staining signal in both K40R and K40Q mutant animals (Figure 4-figure
274 supplement 2A), which is consistent with previous observations in Drosophila (Mao et al., 2017).
275 Neither *mec-12(K40R)* nor *mec-12(K40Q)* mutations generated significant defects in TRN
276 neurite morphogenesis (Figure 4A-B). The only notable defect was that ~20% of PLM-AN failed
277 to produce the synaptic branch in *mec-12(K40Q)* mutants (Figure 4C), suggesting that K40
278 hyperacetylation might affect MT dynamics during neurite branching. Moreover, *mec-12(K40Q)*

279 mutants showed moderately reduced regrowth of PLM-AN after laser axotomy (Figure 4D),
280 suggesting that K40 hyperacetylation might also affect MT functions during axonal regeneration.
281 Previous work found that the α-tubulin acetyltransferase MEC-17 plays an important role
282 in controlling MT number and organization and neurite growth (Cueva et al., 2012; Topalidou et
283 al., 2012). However, no significant downregulation of MEC-12 K40 acetylation was observed in
284 *mec-17(-)* mutants due to the redundancy with another acetyltransferase ATAT-2 (Akella et al.,
285 2010; Topalidou et al., 2012), suggesting that the phenotypes of *mec-17(-)* mutants was not due
286 to the loss of K40 acetylation. Moreover, Topalidou et al. (2012) found that expression of the
287 enzymatically inactive MEC-17(G121W and G123W; termed as dW) mutants rescued some
288 TRN defects of *mec-17(-)* mutants, including the touch sensitivity and the growth of ectopic
289 ALM-PN, whereas Shida et al. (2010) found that the enzymatically dead MEC-17 could not
290 rescue the touch defects. Both studies used exogenous transgenic expression of MEC-17
291 mutants, whose expression levels were uncertain.
292 We created the *mec-17(dW)* allele by editing the endogenous *mec-17* locus and confirmed
293 that MEC-12 K40 acetylation was not significantly reduced upon the loss of enzymatic activity
294 of MEC-17 in *mec-17(dW)* mutants but was completely lost in *mec-17(dW); atat-2(-)* double
295 mutants (Figure 4-figure supplement 2B-C). Importantly, the defects in touch sensitivity found in
296 *mec-17(-)* mutants was not observed in *mec-17(dW)* mutants (Figure 4E), supporting that MEC-
297 17 has separate functions independent of its acetyltransferase activity. This result is consistent
298 with the normal touch sensitivity in *mec-12(K40R)* mutants (Figure 4E) and indicates that K40
299 acetylation is not required for TRN mechanosensation.
300 Furthermore, compared to *mec-17(-)* mutants, the ectopic growth of ALM-PN and the
301 neurite swelling and looping phenotypes, which were caused by MT bending in the absence of
302 MEC-17 (Topalidou et al., 2012), were partially rescued in *mec-17(dW)* mutants (Figure 4F-H).
303 These results supported a non-enzymatic function of MEC-17 in regulating MT organization and
304 neurite outgrowth. Importantly, none of the remaining *mec-17(dW)* defects were found in *mec-*
305 *12(K40R)* mutants, suggesting that even the enzymatic activity of MEC-17 may regulate neurite
306 morphology through an α-tubulin K40-independent mechanism, which may involve the
307 acetylation of other residues of α-tubulin or other proteins. Removing *atat-2* in the *mec-17(-)* and
308 *mec-17(dW)* mutants did not make the neurite morphological defects worse despite eliminating
309 K40 acetylation.

310

311 **Mutation of MEC-7/β-tubulin K252 strongly impairs neurite development**

312 The lack of obvious phenotypes in K40 mutants prompted us to look for other potential
313 tubulin acetylation sites, such as the β-tubulin K252, which was reported to be acetylated by
314 San/Nat5 in human cells (Chu et al., 2011). K252 and flanking residues are highly conserved
315 among β-tubulin isotypes and across species (Figure 4-figure supplement 1B). We created
316 acetyl-mimicking K252Q and unmodifiable K252R mutants by editing the endogenous *mec-7*
317 locus and found that both mutations caused strong neurite growth defects, similar to previously
318 categorized *mec-7(anti)* mutants (Figure 4I-J). All TRN neurites were severely shortened in these
319 mutants with K252R showing a stronger phenotype than K252Q mutants. Previous work
320 suggested that acetylation of K252 reduced the incorporation of tubulin into MTs by neutralizing
321 the positive charge of K252, which is located at the intradimer interface of α/β-tubulins (Chu et
322 al., 2011). Our studies with the acetyl-mimicking K252Q mutants supported this hypothesis, but
323 the K252R results are rather unexpected, as this mutation in theory would not affect the amino
324 acid charge at that position. However, we could not rule out the possibility that substituting
325 lysine with arginine caused conformational change of the tubulin heterodimer, creating
326 dominant-negative effects. Deletion of the *C. elegans* homolog of San/Nat5, *F40F4.7(tm2414)*,
327 did not cause any TRN defects. Thus, it remains unclear what enzyme mediates the K252
328 acetylation of MEC-7 in *C. elegans*.

329

330 **Polyglutamylation on the C-terminal tail of tubulins reduces MT stability and prevents**
331 **excessive neurite growth in TRNs**

332 The C-terminal tail of the tubulins harbors the sites for polymodifications, such as
333 polyglutamylation and polyglycylation, which occur on the glutamic acid residues and regulate
334 the interaction between MTs and various motor proteins and MAPs. Polyglutamylation is
335 associated with stable MTs in cilia, centrioles, mitotic spindles, and axons (Kubo et al., 2010;
336 Lacroix et al., 2010; Suryavanshi et al., 2010), while polyglycylation marks the stable axonemal
337 MTs in flagellated and ciliated cells (Xia et al., 2000). In *C. elegans*, polyglutamylation regulates
338 ciliary microtubule organization in ciliated sensory neurons, but no polyglycylation signal was
339 observed due to the lack of polyglycylase homologs (Kimura et al., 2010).

340 The MEC-12 α-tubulin C-terminal tail consists of 15 amino acids (436-450aa;
341 GVDSMEDNGEEGDEY), and the last 12 (439-450aa) showed significant sequence divergence
342 among the isotypes (Figure 5-figure supplement 1). To understand the function of the C-terminal
343 tail, we first deleted the DNA encoding the last 7 amino acids (ΔGEEGDEY) in the endogenous
344 *mec-12* locus and found that the mutants grew an ectopic ALM-PN (Figure 5A), suggesting that
345 the overall effects of this fragment may be MT-destabilizing and thus their removal induced
346 excessive neurite growth. Changing all 7 amino acids to alanine resulted in similar phenotypes.
347 There are four glutamic acid residues in MEC-12 C-terminal tail and three of them are in the last
348 7 amino acids; these residues are potential sites for polyglutamylation. Mutating any of them to
349 alanine could induce the growth of ALM-PN and converting all to alanine produced the strongest
350 phenotype, suggesting that their functions are additive (Figure 5A-B). Deleting the glutamic acid
351 residues produced similar effects as changing them to alanine. Therefore, we hypothesized that
352 disabling tubulin polyglutamylation increased MT stability, resulting in the growth of an extra
353 neurite. Indeed, the *mec-12(4Es-A)* mutants, in which all four glutamic acids were mutated to
354 alanine, showed significantly reduced number of EBP-2 tracks in sensitized conditions (Figure
355 5C-D), indicating reduced MT dynamics upon the loss of polyglutamylation. Nevertheless, the
356 MT polarity was preserved in the *mec-12(4Es-A)* mutants (Figure 5E).
357 Previous studies found that tubulin polyglutamylation may inhibit axonal regeneration by
358 affecting MT dynamics and the removal of the *ttll-5* gene that codes for a tubulin tyrosine ligase-
359 like protein responsible for polyglutamylation enhanced regeneration (Ghosh-Roy et al., 2012).
360 We found that the *mec-12(4Es-A)* mutants also had enhanced axonal regeneration, which is
361 similar to the *ttll-5(-)* mutants (Figure 5F). Importantly, the *mec-12(4Es-A); ttll-5(-)* double
362 mutants did not show a phenotype stronger than either of the two single mutants (Figure 5G),
363 suggesting that the major function of the four glutamic residues is mediated by
364 polyglutamylation.
365 Tubulin polyglutamylation was found to stimulate spastin-mediated MT severing in
366 human cells (Lacroix et al., 2010). We found, however, that the loss of the *C. elegans* homolog
367 spastin, *spas-1*, did not produce the ALM-PN phenotype (Figure 5H), suggesting that spastin
368 may not mediate the effects of polyglutamylation in the TRNs. On the other hand, the MT-
369 depolymerizing kinesin-13 homolog *klp-7* was found to mediate the effects of polyglutamylation
370 in regeneration (Ghosh-Roy et al., 2012). In fact, we and others have previously found that the

371 loss of *klp-7* led to the growth of an ectopic ALM-PN similar to the *mec-12(4Es-A)* mutants (Puri
372 et al., 2021; Zheng et al., 2017). In this study, we created *klp-7(-); mec-12(4Es-A)* double
373 mutants by inactivating *klp-7* in *mec-12(4Es-A)* animals through Cas9-mediated gene editing
374 since the two genes are on the same chromosome (Figure 5-figure supplement 2). We found that
375 the *klp-7(-); mec-12(4Es-A)* double mutants did not enhance the ALM-PN phenotype of the *klp-*
376 *7(-)* single mutants (Figure 5H), suggesting that MEC-12 polyglutamylation likely acted through
377 KLP-7. Thus, we suspect that tubulin polyglutamylation of the α-tubulin C-terminal tail might
378 enhance the binding of KLP-7 to MTs to increase MT dynamics.
379 Despite the above defects, tubulin polyglutamylation did not affect the transport of
380 cargos, such as the synaptic vesicles and mitochondria, along the axons (Figure 5-figure
381 supplement 3A-C). Unlike the *mec-7(S172A)* mutants, which also grew an ectopic ALM-PN,
382 *mec-12(4Es-A)* animals did not show the transport of cargos into the extra ALM-PN (compare
383 Figure 5-figure supplement 3A-C with Figure 2E and 2G). These results suggest that the MT
384 defects caused by the lack of polyglutamylation may be more subtle than the general alteration of
385 MT dynamics in S172 mutants. Moreover, the touch sensitivity of the *mec-12(4Es-A)* mutants
386 also appeared to be normal, suggesting that polyglutamylation may not be essential for the
387 mechanosensory function of TRNs (Figure 5-figure supplement 3D).
388
389 **Polyglutamylation in the TRN neurites are abolished by mutations in *mec-12* and *mec-7***
390 To confirm that the above mutations affected polyglutamylation, we stained the *in vitro*
391 cultured TRNs with two anti-polyglutamylation antibodies, GT335 and IN105. The former
392 recognized the octapeptide EGEGE(*EE)G containing a branchpoint and a side chain of two
393 glutamyl units (Wolff et al., 1992), and the latter recognized a linear chain of four or more
394 glutamates (Rogowski et al., 2010). Interestingly, IN105 only stained the cell body of TRNs,
395 while GT335 stained both the cell body and the neurites (Figure 6A-B), suggesting that the
396 axonal MTs carry short glutamate side chains containing less than four glutamates. As a control,
397 we also did staining with anti-glycylated tubulin antibodies (Gly-pep1) but did not observe any
398 signal in embryonically derived cells, supporting the absence of polyglycylation in *C. elegans*.
399 Given our focus on neurite growth, we used GT335 in the following studies. As expected,
400 TRNs extracted from *mec-12(4Es-A)* mutants showed a reduction in polyglutamylation signals
401 and further substituting the last three glutamates in the C-terminal tail of MEC-7 with alanine

402 (ADEDAAEAFDGE to ADADAAAAFDGA) abolished the staining signal in the axons (Figure
403 6B-C). Thus, we reasoned that both MEC-12/α-tubulin and MEC-7/β-tubulin were subjected to
404 polyglutamylation.

405 Like MEC-12/α-tubulin, the MEC-7/β-tubulin C-terminal tail also contains 15 amino
406 acids and the last 12 (430-441aa) were divergent among the isotypes (Figure 6-figure supplement
407 1A). Although changing the last three glutamates to alanine removed the polyglutamylation sites
408 on β-tubulin, the *mec-7(3Es-A)* mutations did not induce the growth of a long ALM-PN and did
409 not enhance the growth of ALM-PN in the *mec-12(4Es-A)* mutants (Figure 6F). This result
410 suggests that polyglutamylation on β-tubulin might have weaker effects than polyglutamylation
411 on α-tubulin.

412 *C. elegans* genome contains six tubulin tyrosine ligase-like genes, including *ttll-4*, *-5*, *-9*,
413 *-11*, *-12*, and *-15*. Although *ttll-12* was thought to be the homolog of human TTLL12, which may
414 not have glutamylase activity based on sequence divergence in the TTL domain (van Dijk et al.,
415 2007), it is biochemically uncertain whether *C. elegans* TTLL-12 indeed lacks glutamate ligation
416 activity. So, we included *ttll-12* in our analysis. Based on the single-cell RNA-sequencing data,
417 only *ttll-4*, *5*, and *12* showed significant expression in the TRNs (Figure 6E). To our surprise,
418 triple knockout mutants of the three *ttll* genes only eliminated the anti-polyE signal in the TRN
419 cell bodies but not the axons (Figure 6B and Figure 6-figure supplement 1B). Further deleting
420 *ttll-9* and *ttll-15* to make quintuple mutants did not reduce but actually increased the staining
421 signal in the axons. Similar anticorrelation between the polyglutamylation signals in the cell
422 body and the axons were also seen in the *mec-12(4Es-A); mec-7(3Es-A)* mutants, in which the
423 reduced signal in axons coincided with increased signal in cell bodies (Figure 6C-D). Overall,
424 the above data appeared to suggest that the known *ttll* genes may not be responsible for the
425 tubulin polyglutamylation in the TRN axons.

426 The major phenotype for the *mec-12(4Es-A)* mutant was the generation of a prominent
427 ectopic ALM-PN, which was not observed in either *ttll-4(-)*, *5(-)*, *12(-)* triple mutants or the
428 quintuple mutants that further deleted *ttll-9* and *15* or the sextuple mutants that deleted all six *ttll*
429 genes (Figure 6F). The sextuple mutants also had anti-polyE staining of the TRN axons similar
430 to the triple and quintuple mutants (Figure 6-figure supplement 1C). The phenotypic discrepancy
431 between the tubulin mutants and the *ttll* mutants suggested the existence of other tubulin
432 polyglutamylases or a function of TTLLs that is independent of tubulin glutamylation.

433

434 **MEC-12/α-tubulin detyrosination and Δ2-tubulin modification**

435 α-tubulin detyrosination occurs at the terminal tyrosine residue, and the detyrosination
436 can lead to the removal of the penultimate glutamate residue, generating Δ2-tubulin. α-tubulin
437 detyrosination and its derivate Δ2-tubulin are enriched in stable MTs. Detyrosination of MTs in
438 the axons recruits kinesin-1 motor domain and enhances kinesin-based transport (Konishi and
439 Setou, 2009). Detyrosination also protects MTs from kinesin-13-mediated depolymerization
440 (Peris et al., 2009). We edited endogenous *mec-12* to first create a ΔY450 mutant that in theory
441 would increase detyrosination levels in TRNs, although detyrosinated MTs may be retyrosinated.
442 Second, we generated the MEC-12 Y450A mutant, which mimics permanent detyrosination.
443 Third, we also generated the MEC-12 ΔEY mutant, which mimics permanent Δ2-tubulin.

444 We did not observe overt defects in TRN morphogenesis in the ΔY450, Y450A, and
445 ΔEY mutants, although they all showed a short ectopic ALM-PN, indicating increased MT
446 stability (Figure 7A). These results are consistent with the fact that detyrosination and Δ2-tubulin
447 modification contribute to stability of MTs possibly by reducing the interaction with KLP-
448 7/kinesin-13. Importantly, we observed combinatorial and additive effects between
449 detyrosination and polyglutamylation, as the deletion of the terminal EY and the two Es in the
450 GEEG motif that are subjected to polyglutamylation created a phenotype that was stronger than
451 either ΔEY or ΔEE mutants (Figure 7A). The length of the ectopic ALM-PN in ΔEE&EY
452 appeared to be the sum of the two single mutants.

453 Tubulin detyrosination is catalyzed by the tubulin carboxypeptidases, vasohibins
454 (VASH1/VASH2), and their stabilizing chaperone SVBP (Nieuwenhuis et al., 2017). Vasohibins
455 have no clear homologs in *C. elegans*, raising the question whether detyrosination occurs in *C.*
456 *elegans*. To test this, we stained the animals with anti-tyrosinated and anti-detyrosinated α-
457 tubulin antibodies. Using the anti-tyrosination antibodies raised against GGY, we were only able
458 to observe weakly stained TRN cell bodies in the wild-type animals but never in the ΔY450,
459 Y450A, and ΔEY mutants (Figure 7B). Using the anti-detyrosination antibodies raised against
460 GEEEGE, we could consistently observe weak staining signals in the TRNs and stronger signals
461 in ΔY450 and Y450A, suggesting that the mutations indeed changed detyrosination levels in the
462 neurons (Figure 7C-D). Interestingly, the ΔEY mutants showed weaker signal than the wild-type,

463 likely because the terminal E of the epitope is removed from the protein, affecting the
464 recognition by the antibodies. Our work is consistent with previous findings that mutating the
465 terminal Y to A in TBA-1 and TBA-2 caused defects in the centration and rotation of centrosome
466 in early embryos (Barbosa et al., 2017), suggesting that tyrosination/detyrosination state of
467 tubulins may indeed regulate MT dynamics in *C. elegans*, although the enzymes that catalyze
468 these PTMs remain elusive.
469

470 **Discussion**

471 **Analyzing the function of tubulin PTMs in neurons with gene editing**

472 Compared to other cell types, microtubules in neurons are highly decorated with a range
473 of tubulin PTMs, including acetylation, polyglutamylation, detyrosination, and Δ2 modifications
474 (Janke and Magiera, 2020). Whether these PTMs are simply markers for mature neurons or play
475 important functions during neuronal differentiation is not entirely clear. In this study, we
476 established an *in vivo* model to test the functional relevance of tubulin PTM by editing the
477 endogenous loci of neuron type-specific tubulin genes to install PTM-mimicking or
478 nonmodifiable mutations. Leveraging the ease of genetic engineering in *C. elegans* and the
479 simple morphology and functional readout of the mechanosensory TRNs, we investigated the
480 role of several tubulin PTMs in axonal growth and regeneration at the single-cell level. In
481 general, two large categories of tubulin PTMs were found (Figure 8). One category, such as β-
482 tubulin S172 phosphorylation and K252 acetylation, has strong impact on neuronal
483 morphogenesis by affecting the incorporation of tubulin heterodimers; the other category, such
484 as tubulin polyglutamylation and detyrosintion, has subtle effects on neurite development by
485 possibly altering the interaction between MTs and MAPs. One clear theme that stemmed from
486 these analyses is that normal neuronal development requires an optimal level of tubulin PTMs.
487 Either the complete absence or the excessive accumulation of tubulin PTMs would cause
488 developmental defects.

489 For example, eliminating S172 phosphorylation through S172A mutation led to the
490 formation of hyperstable MTs and ectopic neurite growth, whereas mimicking permanent
491 phosphorylation through S172E mutation resulted in highly dynamic MTs, disrupted MT
492 polarity, and strongly impaired neurite development. Both mutations impaired axonal
493 regeneration and caused defects in MT-dependent cargo transport. Previous studies found that

494 S172-phosphorylated tubulin dimers cannot be incorporated into growing MTs (Fourest-Lieuvin
495 et al., 2006). The fact that S172E mutants showed an antimorphic gain-of-function phenotype
496 (indicated by severe neurite growth defects) instead of a loss-of-function phenotype (moderate
497 growth defects found in S172P and *mec-7(-)* mutants) suggested that hyperphosphorylation did
498 not simply inactivate the tubulin but produced dominant-negative effects. We suspect that MEC-
499 7(S172E) proteins may form non-functional heterodimers with all α-tubulin isotypes expressed
500 in TRNs and thus disabling all tubulins for MT polymerization, causing strong phenotypes. In
501 contrast, the lack of MEC-7 in the deletion mutants may be partly compensated by other β-
502 tubulin isotypes, resulting in a less severe phenotype.
503 *mec-7*/β-tubulin K252 acetylation serves as another example for the requirement of
504 optimal PTM levels, as both the acetyl-mimicking K252Q and the unmodifiable K252R mutants
505 caused antimorphic phenotypes. Chu et al. (2011) previously found that acetylation of K252
506 slowed down tubulin incorporation into MTs, which is consistent with K252Q phenotype. But
507 the stronger defects in K252R mutants suggested that the complete elimination of K252
508 acetylation may cause more severe consequence on MT stability. Nevertheless, we could not rule
509 out the possibility that K252R mutation induced structural changes of tubulin heterodimer
510 independently of disabling K252 acetylation.
511
512 **α-tubulin K40 acetylation has little effects on neuronal differentiation**
513 Although α-tubulin K40 acetylation serves as a marker for stable MTs in neurons,
514 whether its relationship with MT stability is correlative or causative remains elusive. The loss of
515 tubulin K40 acetyltransferase MEC-17 caused a range of defects in MT structure and
516 organization, neurite development, and touch sensation in *C. elegans* (Topalidou et al., 2012).
517 Drosophila α-tubulin acetylase also appeared to be required for mechanosensation in the larval
518 peripheral nervous system (Yan et al., 2018). However, mouse lacking the acetyltransferase
519 ATAT1 or the deacetylase HDAC6 did not show obvious defects in neuronal development and
520 functions (Kalebic et al., 2013; Kim et al., 2013). Moreover, despite *in vivo* evidence for the
521 correlation of acetylation level with binding of motor protein and cargo transport in neurons
522 (Reed et al., 2006), *in vitro* assays found that motor motility was not affected by acetylation
523 status (Kaul et al., 2014). Since K40 is located in the MT lumen, its acetylation may not directly
524 affect MAP binding.

525 By editing the endogenous locus of the only α-tubulin gene that codes for a K40-
526 containing isotype, we partly solved the controversy in *C. elegans* by finding a lack of
527 acetyltransferase mutant phenotypes in the non-acetylatable tubulin mutants. None of the
528 morphological and functional defects in *mec-17(-)* mutants were observed in *mec-12(K40R)*
529 mutants and only some were observed in *mec-17* enzymatically dead mutants, suggesting that
530 MEC-17 likely functions by acetylating other substrates and/or acts independently of its
531 enzymatic activity. The discrepancy between the phenotypes of *mec-17(-)* and *mec-12* K40
532 mutants highlights the need of directly assessing the effects of tubulin PTMs through
533 endogenous gene editing.
534 Although our results argued against a causative relationship between K40 acetylation and
535 MT stability during neuronal development, we could not rule out effects of K40 acetylation in
536 other cellular conditions. For example, excessive acetylation in *mec-12(K40Q)* mutants appeared
537 to limit the ability of the axons to branch and regenerate, indicating that acetylation may reduce
538 polymerization dynamics when they were needed in response to external cues or stress. In
539 addition, previous studies found that K40 acetylation increased mechanical resilience against
540 damages caused by repetitive bending, thus protecting MTs from mechanical aging (Portran et
541 al., 2017; Xu et al., 2017). Such function may be important in preserving axon integrity during
542 neuronal aging. In fact, Neumann and Hilliard (2014) found that the loss of MEC-17 led to an
543 age-related, adult-onset, and progressive axonal degeneration, but this phenotype appeared to be
544 independent of MEC-17-mediated tubulin acetylation. Thus, whether K40 acetylation plays a
545 role in neuronal aging awaits further investigation.
546
547 **Polyglutamylation and tyrosination promotes MT dynamics likely by recruiting kinesin-13**
548 The C-terminal tail of tubulin, which protrudes from the MT surface, serves as a hotspot
549 for PTMs that regulate the dynamic properties of MTs by fine-tuning their interaction with
550 MAPs. For example, *in vitro* studies in a recombinant system found that the motility of kinesin
551 motors were regulated by polyglutamylation, and the length of the glutamate side chain
552 determined the type of kinesin motor that were activated (Sirajuddin et al., 2014). Similarly,
553 detyrosination enhanced the interaction with kinesin-2 and kinesin-7 motor proteins, thus
554 increasing their motility and processivity on MTs (Barisic et al., 2015; Sirajuddin et al., 2014). In
555 our studies, we found that eliminating polyglutamylation or installing permanent detyrosination

556 through the editing of α-tubulin locus increased MT stability and caused ectopic neurite growth.
557 Genetic studies suggested that these effects are likely caused by reduced interaction with the
558 MT-depolymerizing kinesin-13 motor protein, since the loss of kinesin-13 generated similar
559 phenotypes, which was not enhanced by the tubulin PTM mutations. Moreover, our results are
560 consistent with previous findings that kinesin-13 and polyglutamylation function in the same
561 pathway to restrict axonal regeneration (Ghosh-Roy et al., 2012), while detyrosination was
562 known to reduce the interaction with kinesin-13 (Peris et al., 2009). Thus, at least in *C. elegans*
563 TRNs, both polyglutamylation and tyrosination seem to promote MT dynamics by enhancing the
564 recruitment of kinesin-13. In fact, we observed additive effects of the two PTMs in double
565 mutants that disabled both polyglutamylation and tyrosination.
566 Interestingly, removing the polyglutamylation sites in MEC-7/β-tubulin did not produce
567 any defects and did not exacerbate the phenotypes of the *mec-12* mutants with no
568 polyglutamylation sites, suggesting functional differences of the PTM on α- and β-tubulin.
569 Previous studies found that α-tubulin polyglutamylation was abundant at all stages of neuronal
570 development in mouse brain and in culture, whereas β-tubulin polyglutamylation only
571 accumulated in mature neurons and was less abundant in general (Audebert et al., 1994). So, the
572 higher abundance of α-tubulin polyglutamylation may explain the stronger effects. Alternatively,
573 it is also possible that glutamylation on the C-terminal tail of the α-tubulin had stronger
574 structural influences on kinesin-13 binding compared to the modification of the β-tubulin.
575 However, the enzymes that mediate polyglutamylation and tyrosination in the TRNs
576 remain elusive. Deletion of the *ttll* enzymes did not eliminate the polyglutamylation signals in
577 the TRN axons and did not cause the ectopic growth of ALM-PN as the removal of
578 polyglutamylation sites did. Although *C. elegans* contains tubulin carboxypeptidases (CCPP-1
579 and CCPP-6) that catalyze deglutamylation (Ghosh-Roy et al., 2012; Kimura et al., 2010; Klimas
580 et al., 2023; O'Hagan et al., 2011), there is no *C. elegans* homolog of the known tubulin
581 detyrosinase. Further studies are needed to identify the potential enzymes that catalyze these
582 tubulin PTMs.
583
584 **Materials and Methods**
585 **Strains and transgenes**

586 *C. elegans* strains were maintained at 20°C as previously described (Brenner, 1974).
587 Strains used in this study were listed in Supplemental File 1. Some strains were provided by the
588 Caenorhabditis Genetics Center (CGC) or by the National BioResource Project (NBRP) of
589 Japan. Transgenes *uIs115[mec-17p::TagRFP] IV*, *uIs134[mec-17p::TagRFP] V*, *uIs31[mec-*
590 *17p::GFP] III*, and *zdIs5[mec-4p::GFP] I* were used to visualize TRNs. Transgene *jsIs609*
591 *[mec-7p::mitoGFP]* and *jsIs821[mec-7p::GFP::rab-3] X* was used to visualize the transport of
592 mitochondria and synaptic vesicles; transgene *juIs338 [mec-4p::ebp-2::GFP + ttx-3p::RFP]* was
593 used to track the dynamics of MTs. For *hpk-1* promoter-reporter, we cloned a 5-kb promoter
594 sequence upstream of the start codon of *B* isoform of *hpk-1* and inserted it into pPD95.75 to
595 make *hpk-1p::GFP*, which was then injected into worms to create *unkEx194 [hpk-1Bp::GFP;*
596 *unc-119(+)]*. To conduct TRN-specific RNAi, we cloned the sense (without start codon) and
597 antisense sequence of *mbk-2* and placed them downstream of a 1.9 kb TRN-specific *mec-17*
598 promoter; both constructs were injected together to create the *unkEx101[mec-17p::mbk-2-*
599 *dsRNA; ceh-22p::GFP]* transgene. OD2984 *ItSi953 [mec-18p::vhhGFP4::Zif-1] II* strain was
600 used for TRN-specific protein degradation.
601
602 **CRISPR/Cas9-mediated gene editing**
603 We adapted a previously published method for CRISPR/Cas9-medicated gene editing
604 (Dokshin et al., 2018). Optimal single guide RNA (sgRNA) targets were found using the online
605 tool CHOPCHOP (https://chopchop.cbu.uib.no/). The sgRNAs were synthesized using the NEB
606 EnGen sgRNA Synthesis Kit (E3322S) and purified using NEB Monarch RNA Cleanup Kit
607 (T2030L). 1 μg of the sgRNA was complexed with 20 pmol recombinant Cas9 endonuclease
608 (NEB # M0646T) and injected into the *C. elegans* gonads with 1 μg single-stranded DNA donors
609 as repair templates for precise editing through homologous recombination. Synonymous
610 mutations were introduced in the repair template. Successful edits were first identified by single-
611 worm PCR and then verified by Sanger sequencing. For each edit, two or three independent lines
612 were obtained and examined. To create genetic knockouts, we selected Cas9 targets in the
613 beginning exons and designed repair templates containing frameshift-causing small deletions.
614 The CRISPR targets and repair templates used for each editing are listed in Supplemental File 2.
615
616 **Microscopy and statistical analysis**

617 Unless otherwise stated, all strains subjected to data collection were bleached and grown
618 at 20 °C for 3 days on nematode growth medium (NGM) agar plates seeded with *E. coli* OP50
619 bacteria. Young adults were anesthetized on 3% agarose pads containing 3% 2,3-Butanedione
620 monoxime (BDM) and imaged using a Leica DMi8 microscope equipped with K5 sCMOS
621 Camera. Measurements of neurite length and fluorescence intensity were made by LAS X
622 software. To compare fluorescence intensity, strains were prepared simultaneously and imaged at
623 the same settings (e.g., 100-ms exposure). In general, at least 40 worms were examined for each
624 strain. Statistical analysis of one-way ANOVA followed by Dunnett's multiple comparisons test
625 of different mutants with the wild-type animals or a Tukey's honestly significant difference
626 (HSD) test for all pairs of conditions was performed using GraphPad Prism 8. Data were plotted
627 as mean ± SD, and adjusted p value < 0.05, 0.01, 0.001, and 0.0001 were indicated by one, two,
628 three, and four asterisks, respectively.
629
630 **Laser Axotomy and axonal regeneration**
631 Laser-mediated axonal cutting was adapted from a previous study (Neumann et al.,
632 2015). Polystyrene microspheres (Polysciences #00876-15; 5-fold dilution) were used to
633 immobilize late-L4 animals on 10% agarose pads. PLM axons were cut 50 µm anterior to the cell
634 body, using a Pulsed Laser Unit attached to the Infinity Scanner on a Leica DMi8 using 63x
635 water lenses. To minimize injury, the lowest energy that enabled the generation of a 2- to 3-µm
636 gap on the axon was used. Animals were then rescued and placed on NGM plates for recovery
637 and were imaged 24 hours after the axotomy. We considered two categories of axonal
638 regeneration: 1) reconnection, which means the proximal and distal axon segments were
639 connected and the connection was clearly visualized in the same focal plane; 2) regrowth, which
640 means that the proximal segment did not reconnect with the distal segment and the distal axon
641 was often degenerated. Only the regrowth cases were used to calculate the average regrowth
642 length, which is the length of the longest regenerative branch from the cut site.
643
644 **Microtubule dynamics analysis**
645 Day-one adult animals expressing *ebp-2::GFP* in the TRNs were immobilized as stated
646 above and imaged with 500-ms exposure continuously for 60 s (i.e. one frame every 529 ms and
647 115 frames in total were collected). ImageJ was used to generate kymographs by placing a 50-

648 μm ROI on PLM-AN starting from the cell body, and the number of EBP comets in the distal 30-
649 μm segment were counted for quantification (we found the 20-μm proximal segment near the
650 cell body sometimes contained many very short EBP comets, obscuring the counting). To
651 increase MT dynamics in some strains, we used a mild colchicine treatment previously reported
652 (Hsu et al., 2014). L4 animals were first transferred to seeded NGM plates containing 0.125 mM
653 colchicine and grown on these plates for 6.5 hours before being transferred back to normal NGM
654 plates for recovery. After a one-hour recovery, the animals were mounted for video recording.
655
656 **Recombinant proteins and kinase assays**
657 Recombinant *C. elegans* MEC-12/MEC-7 tubulin dimers and MBK-2 kinase were
658 produced in insect cells using the baculovirus-insect protein expression system. The *Spodoptera*
659 *frugiperda* Sf9 cells (Thermo #11496015) were used to generate and propagate recombinant
660 baculoviruses, and the *Trichoplusia ni* ovary High Five cells (Thermo #B85502) were used for
661 protein expression. For the tubulins, the cDNA sequences encoding MEC-12 and MEC-7 were
662 codon-optimized for expression in High Five cells, and the recombinant tubulin heterodimer
663 were generated using a previously published protocol (Ti et al., 2020).
664 For MBK-2, we cloned the cDNA of the *m* isoform of MBK-2 (NP_001293914.1) into
665 the pACEBac1 vector and infected the High Five cells with P3 virus. About 60 hours after the
666 infection, cells were harvested by centrifugation (1,000 g, 15 minutes) and lysed in lysis buffer
667 (50 mM Tris-HCl, 20 mM imidazole, 500 mM KCl, 1 mM $MgCl_2$, 0.5 mM β-mercaptoethanol, 1
668 mM ATP, 1% IGEPAL, 5% glycerol, 3 U/ml Benzonase and Roche Complete EDTA-free
669 protease inhibitor, pH 8.0) using dounce homogenization (20 strokes) on ice or at 4°C. The
670 extracts were clarified by centrifugation at 55,000 rpm for 1 hour. Supernatant was then filtered
671 through the 0.22 μm Millex-GP PES membrane (Millipore) and loaded onto HisTrap HP
672 column. After washing the HisTrap HP column with lysis buffer till the absorbance at 280 nm
673 reaches the baseline, the bound protein was eluted with elution buffer (25 mM Tris-HCl, 250
674 mM imidazole, 500 mM KCl, 1 mM $MgCl_2$, 2 mM β-mercaptoethanol, 1 mM ATP, 5% glycerol,
675 pH 8.0). The eluate was mixed with TEV protease (final 0.75 mg/ml) and dialyzed against low
676 salt buffer (25 mM Tris-HCl, 20 mM imidazole, 100 mM KCl, 1 mM $MgCl_2$, 2 mM β-
677 mercaptoethanol, 1 mM ATP, 5% glycerol, pH 8.0) for 18 hours. The dialyzed protein solution
678 was then loaded onto HisTrap HP and HiTrap Q FF columns. After washing the columns with

679 low salt buffer, the HisTrap HP column was disconnected, and the HiTrap Q FF column was
680 eluted with a 0-100% gradient to the high salt buffer (25 mM Tris-HCl, 20 mM imidazole, 500
681 mM KCl, 1 mM $MgCl_2$, 2 mM β-mercaptoethanol, 1 mM ATP, 5% glycerol, pH 8.0). The
682 fractions containing MBK-2m were collected and loaded onto a Superdex 75 16/60 column
683 (Cytiva #28989333) equilibrated in the size-exclusion buffer (1X BRB80, 5% glycerol, 1 mM
684 ATP, 2 mM β-mercaptoethanol, pH 6.8). The peak fractions were pooled for SDS-PAGE
685 analysis and mass spectrometry characterization.
686 The kinase assay was performed as previously described (Fourest-Lieuvin et al., 2006;
687 Ori-McKenney et al., 2016). 500 nM recombinant MEC-12/MEC-7 tubulins and a kinase
688 candidate [500 nM recombinant MBK-2m or 475 nM CDK1/Cyclin B (Thermo Fisher; Cat#
689 PV3292)] were incubated in MEM buffer [100 mM MES, pH 6.7, 1 mM EGTA, 1 mM $MgCl_2$,
690 0.1 mM DTT] supplemented with 5 mM $MgCl_2$ and 1 mM ATP or BRB80 buffer (80 mM
691 PIPES, 1 mM $MgCl_2$, and 1 mM EGTA, pH 6.8) supplemented with 1 mM DTT, 1 mM PMSF,
692 and 1 mM ATP at 30°C for 1 hour. Reaction controls were set up by replacing the kinase or
693 tubulins with water. Samples were boiled for 10 min and analyzed by western blot using the anti-
694 phospho-S172 antibodies (abcam #ab76286; 1:3000 diluted in TBST buffer) and the anti-α-
695 tubulin antibodies (abcam #ab7291; for loading controls) as the primary antibodies.
696
697 **Immunofluorescence**
698 To detect tubulin PTM signals in the animals, we conducted immunofluorescent staining
699 using a previously published protocol (Finney and Ruvkun, 1990). Briefly, worms fixed in 2%
700 formaldehyde (in Ruvkun Finney Buffer) were subjected to three cycles of freeze-and-thaw.
701 After washing twice with Tris-Triton Buffer (TTB; 100 mM Tris-HCl pH 7.4, 1% Triton X-100,
702 1 mM EDTA), worms were treated with 1% β-mercaptoethanol in TTB at 37°C with gentle
703 agitation for 4 hours. Samples were then washed with Borate buffer (25 mM H_3BO_3, 25 mM
704 NaOH, pH 9.2) and incubated in borate buffer with 10 mM DTT at 37°C and in borate buffer
705 with 0.3% H_2O_2 at room temperature, sequentially; each incubation lasted 15 min under agitation
706 and was followed by a wash using borate buffer. At this stage, worms were permeable to
707 macromolecules due to the reduction of cuticular disulfide bonds to -SH and the subsequent
708 oxidation of -SH to $-SO_3$. Permeabilized worms were then blocked with Antibody Buffer (PBST
709 containing 1% BSA and 1 mM EDTA) for 1 h and incubated with antibodies at a 1:100 (for

710 primary antibody) or 1:1000 (for secondary antibodies) dilution in Antibody Buffer for 2 hours.
711 Three washes with shaking for a total of 2 hours were applied after antibody incubation.
712 Antibodies used in this study included the anti-phospho-S172 (abcam; #ab76286), anti-
713 acetyl-K40 (abcam; #ab24610), anti-polyE GT335 (AdipoGen Life Science; #AG-20B-0020-
714 C100), anti-polyE chain IN105 (AdipoGen; #AG-25B-0030-C050), anti-glycylated tubulin Gly-
715 pep1 (AdipoGen; AG-25B-0034-C100), anti-tyrosinated α-tubulin (Sigma; #MAB1864-I), anti-
716 detyrosinated α-tubulin (Sigma; #MAB5566), and fluorophore-labeled secondary antibodies
717 from Thermo Fisher (#A32723 and #A11006) and Jackson ImmunoResearch (#115-025-164,
718 #111-545-003, #111-025-003, and #115-545-003).
719
720 ***In vitro* culture of *C. elegans* embryonic cells**
721 *C. elegans* embryos were collected from gravid adults through a bleaching procedure,
722 washed with M9 buffer and then egg buffer (118 mM NaCl, 48 mM KCl, 3.4 mM CaCl2, 3.4
723 mM MgCl2, 5 mM Hepes, pH 7.4), and incubated in egg buffer (1 ml per 100 µl egg pellet)
724 supplemented with 0.5% chitinase (Sigma #C6137) for ~20 minutes until the eggshells were
725 dissolved. Digested embryos were washed in egg buffer twice and subsequently in L-15CM
726 medium [Leibovitz's L-15 Medium (Thermo Fisher #11415064) supplemented with 10% FBS,
727 100 U/ml penicillin-streptomycin (Sigma; P4333), and 0.85% sucrose]. Cells were dissociated in
728 L-15CM using a 25-gauge needle and then adhered to slides pre-coated with 0.5 mg/ml lectin
729 (Sigma #L0881) and 0.01 mg/ml poly-D-lysine (Thermo Fisher #A3890401). After 1 hour of
730 adhesion, more L-15CM medium was added to the petri dish to submerge the slides and to
731 support the growth of cells, which were examined 24 hours later.
732 For the subsequent immunostaining, cells were carefully washed with PBS twice, fixed
733 with 4% formaldehyde in PBS for 8 min, and washed with ice-cold PBS. They were then
734 permeabilized using PBST (0.1% Triton X-100 in PBS) for 10 min, blocked in the blocking
735 buffer (4% BSA in PBST) for 30 min, and stained with antibodies (1:1000 dilution) in the
736 blocking buffer for 2 hours; PBST wash was conducted 5 times after each step above. Slides
737 were mounted using VECTASHIELD Antifade Mounting Medium (Vector Laboratories #H-
738 1000), and coverslips were sealed by nail polish before imaging. In order to identify the TRNs
739 among the embryonic cells, we used animals carrying a TRN marker *mec-17p::TagRFP* for the

740 experiments and the cells that express RFP were identified as TRNs. Nevertheless, we could not
741 distinguish the TRN subtypes in cell culture.
742

743 **Acknowledgement**

744 We thank the Caenorhabditis Genetics Center, which is funded by the National Institutes of
745 Health (NIH) Office of Research Infrastructure Programs (P40 OD010440), and the National
746 BioResource Project (NBRP), which is funded by the Japanese government, for providing
747 strains. We thank Nina Peel for providing some *ttll* mutants. We thank Rui Wang in the Zheng
748 lab for technical assistance in staining the embryonically derived TRNs. We thank Paige Wilson
749 for technical assistance in creating the *mec-7* S172 mutants in the Martin Chalfie lab at Columbia
750 University. This study was supported by funds from the National Natural Science Foundation of
751 China (Excellent Young Scientists Fund for Hong Kong and Macau 32122002 to C.Z.), the
752 Research Grant Council of Hong Kong [ECS 27104219, GRF 17107021, GRF 17106322, and
753 CRF C7026-20G to C.Z., and C7064-22GF to S.-C.T.], the Food and Health Bureau of Hong
754 Kong [HMRF 07183186 and 09201426 to C.Z.], and the seed fund from the University of Hong
755 Kong [201910159087 and 202011159053 to C.Z.].
756

757 **References**

758 Akagawa, R., Y.I. Nabeshima, and T. Kawauchi. 2021. Alternative Functions of Cell Cycle-Related
759 and DNA Repair Proteins in Post-mitotic Neurons. *Front Cell Dev Biol*. 9:753175.
760 Akella, J.S., D. Wloga, J. Kim, N.G. Starostina, S. Lyons-Abbott, N.S. Morrissette, S.T. Dougan, E.T.
761 Kipreos, and J. Gaertig. 2010. MEC-17 is an alpha-tubulin acetyltransferase. *Nature*.
762 467:218-222.
763 Audebert, S., A. Koulakoff, Y. Berwald-Netter, F. Gros, P. Denoulet, and B. Edde. 1994.
764 Developmental regulation of polyglutamylated alpha- and beta-tubulin in mouse brain
765 neurons. *J Cell Sci*. 107 (Pt 8):2313-2322.
766 Barbosa, D.J., J. Duro, B. Prevo, D.K. Cheerambathur, A.X. Carvalho, and R. Gassmann. 2017.
767 Dynactin binding to tyrosinated microtubules promotes centrosome centration in C.
768 elegans by enhancing dynein-mediated organelle transport. *PLoS Genet*. 13:e1006941.
769 Barisic, M., R. Silva e Sousa, S.K. Tripathy, M.M. Magiera, A.V. Zaytsev, A.L. Pereira, C. Janke, E.L.
770 Grishchuk, and H. Maiato. 2015. Mitosis. Microtubule detyrosination guides
771 chromosomes during mitosis. *Science*. 348:799-803.
772 Brenner, S. 1974. The genetics of Caenorhabditis elegans. *Genetics*. 77:71-94.
773 Chalfie, M., and J.N. Thomson. 1979. Organization of neuronal microtubules in the nematode
774 Caenorhabditis elegans. *J Cell Biol*. 82:278-289.

775 Chalfie, M., and J.N. Thomson. 1982. Structural and functional diversity in the neuronal
776 microtubules of Caenorhabditis elegans. *J Cell Biol*. 93:15-23.
777 Chang, J., R.H. Baloh, and J. Milbrandt. 2009. The NIMA-family kinase Nek3 regulates
778 microtubule acetylation in neurons. *J Cell Sci*. 122:2274-2282.
779 Chu, C.W., F. Hou, J. Zhang, L. Phu, A.V. Loktev, D.S. Kirkpatrick, P.K. Jackson, Y. Zhao, and H.
780 Zou. 2011. A novel acetylation of beta-tubulin by San modulates microtubule
781 polymerization via down-regulating tubulin incorporation. *Mol Biol Cell*. 22:448-456.
782 Cueva, J.G., J. Hsin, K.C. Huang, and M.B. Goodman. 2012. Posttranslational acetylation of
783 alpha-tubulin constrains protofilament number in native microtubules. *Curr Biol*.
784 22:1066-1074.
785 Dokshin, G.A., K.S. Ghanta, K.M. Piscopo, and C.C. Mello. 2018. Robust Genome Editing with
786 Short Single-Stranded and Long, Partially Single-Stranded DNA Donors in Caenorhabditis
787 elegans. *Genetics*. 210:781-787.
788 Even, A., G. Morelli, L. Broix, C. Scaramuzzino, S. Turchetto, I. Gladwyn-Ng, R. Le Bail, M. Shilian,
789 S. Freeman, M.M. Magiera, A.S. Jijumon, N. Krusy, B. Malgrange, B. Brone, P. Dietrich, I.
790 Dragatsis, C. Janke, F. Saudou, M. Weil, and L. Nguyen. 2019. ATAT1-enriched vesicles
791 promote microtubule acetylation via axonal transport. *Sci Adv*. 5:eaax2705.
792 Finney, M., and G. Ruvkun. 1990. The unc-86 gene product couples cell lineage and cell identity
793 in C. elegans. *Cell*. 63:895-905.
794 Fourest-Lieuvin, A., L. Peris, V. Gache, I. Garcia-Saez, C. Juillan-Binard, V. Lantez, and D. Job.
795 2006. Microtubule regulation in mitosis: tubulin phosphorylation by the cyclin-
796 dependent kinase Cdk1. *Mol Biol Cell*. 17:1041-1050.
797 Ghosh-Roy, A., A. Goncharov, Y. Jin, and A.D. Chisholm. 2012. Kinesin-13 and tubulin
798 posttranslational modifications regulate microtubule growth in axon regeneration. *Dev
799 Cell*. 23:716-728.
800 Hsu, J.M., C.H. Chen, Y.C. Chen, K.L. McDonald, M. Gurling, A. Lee, G. Garriga, and C.L. Pan.
801 2014. Genetic analysis of a novel tubulin mutation that redirects synaptic vesicle
802 targeting and causes neurite degeneration in C. elegans. *PLoS Genet*. 10:e1004715.
803 Jaglin, X.H., K. Poirier, Y. Saillour, E. Buhler, G. Tian, N. Bahi-Buisson, C. Fallet-Bianco, F. Phan-
804 Dinh-Tuy, X.P. Kong, P. Bomont, L. Castelnau-Ptakhine, S. Odent, P. Loget, M.
805 Kossorotoff, I. Snoeck, G. Plessis, P. Parent, C. Beldjord, C. Cardoso, A. Represa, J. Flint,
806 D.A. Keays, N.J. Cowan, and J. Chelly. 2009. Mutations in the beta-tubulin gene TUBB2B
807 result in asymmetrical polymicrogyria. *Nat Genet*. 41:746-752.
808 Janke, C. 2014. The tubulin code: molecular components, readout mechanisms, and functions. *J
809 Cell Biol*. 206:461-472.
810 Janke, C., and M.M. Magiera. 2020. The tubulin code and its role in controlling microtubule
811 properties and functions. *Nat Rev Mol Cell Biol*. 21:307-326.
812 Kalebic, N., S. Sorrentino, E. Perlas, G. Bolasco, C. Martinez, and P.A. Heppenstall. 2013.
813 alphaTAT1 is the major alpha-tubulin acetyltransferase in mice. *Nat Commun*. 4:1962.
814 Kaul, N., V. Soppina, and K.J. Verhey. 2014. Effects of alpha-tubulin K40 acetylation and
815 detyrosination on kinesin-1 motility in a purified system. *Biophys J*. 106:2636-2643.
816 Kim, A.H., and A. Bonni. 2008. Cdk1-FOXO1: a mitotic signal takes center stage in post-mitotic
817 neurons. *Cell Cycle*. 7:3819-3822.

818 Kim, G.W., L. Li, M. Ghorbani, L. You, and X.J. Yang. 2013. Mice lacking alpha-tubulin
819 acetyltransferase 1 are viable but display alpha-tubulin acetylation deficiency and
820 dentate gyrus distortion. *J Biol Chem*. 288:20334-20350.
821 Kimura, Y., N. Kurabe, K. Ikegami, K. Tsutsumi, Y. Konishi, O.I. Kaplan, H. Kunitomo, Y. Iino, O.E.
822 Blacque, and M. Setou. 2010. Identification of tubulin deglutamylase among
823 Caenorhabditis elegans and mammalian cytosolic carboxypeptidases (CCPs). *J Biol Chem*.
824 285:22936-22941.
825 Kirszenblat, L., B. Neumann, S. Coakley, and M.A. Hilliard. 2013. A dominant mutation in mec-
826 7/beta-tubulin affects axon development and regeneration in Caenorhabditis elegans
827 neurons. *Mol Biol Cell*. 24:285-296.
828 Klimas, A.S., J. Dominguez, B.P. Shah, Z.Y. Lee, and N. Peel. 2023. The C. elegans deglutamylase
829 CCPP-6 does not operate redundantly with CCPP-1 in gross cilia integrity. *MicroPubl Biol*.
830 2023.
831 Konishi, Y., and M. Setou. 2009. Tubulin tyrosination navigates the kinesin-1 motor domain to
832 axons. *Nat Neurosci*. 12:559-567.
833 Kubo, T., H.A. Yanagisawa, T. Yagi, M. Hirono, and R. Kamiya. 2010. Tubulin polyglutamylation
834 regulates axonemal motility by modulating activities of inner-arm dyneins. *Curr Biol*.
835 20:441-445.
836 Lacroix, B., J. van Dijk, N.D. Gold, J. Guizetti, G. Aldrian-Herrada, K. Rogowski, D.W. Gerlich, and
837 C. Janke. 2010. Tubulin polyglutamylation stimulates spastin-mediated microtubule
838 severing. *J Cell Biol*. 189:945-954.
839 Lee, H.M.T., N.Y. Sayegh, A.S. Gayek, S.L.J. Jao, M. Chalfie, and C. Zheng. 2021. Epistatic,
840 synthetic, and balancing interactions among tubulin missense mutations affecting
841 neurite growth in Caenorhabditis elegans. *Mol Biol Cell*. 32:331-347.
842 Lin, Z., I. Gasic, V. Chandrasekaran, N. Peters, S. Shao, T.J. Mitchison, and R.S. Hegde. 2020.
843 TTC5 mediates autoregulation of tubulin via mRNA degradation. *Science*. 367:100-104.
844 Lu, Y.M., and C. Zheng. 2022. The Expression and Function of Tubulin Isotypes in Caenorhabditis
845 elegans. *Front Cell Dev Biol*. 10:860065.
846 Mao, C.X., X. Wen, S. Jin, and Y.Q. Zhang. 2017. Increased acetylation of microtubules rescues
847 human tau-induced microtubule defects and neuromuscular junction abnormalities in
848 Drosophila. *Dis Model Mech*. 10:1245-1252.
849 Neumann, B., S. Coakley, R. Giordano-Santini, C. Linton, E.S. Lee, A. Nakagawa, D. Xue, and M.A.
850 Hilliard. 2015. EFF-1-mediated regenerative axonal fusion requires components of the
851 apoptotic pathway. *Nature*. 517:219-222.
852 Neumann, B., and M.A. Hilliard. 2014. Loss of MEC-17 leads to microtubule instability and
853 axonal degeneration. *Cell Rep*. 6:93-103.
854 Nieuwenhuis, J., A. Adamopoulos, O.B. Bleijerveld, A. Mazouzi, E. Stickel, P. Celie, M. Altelaar, P.
855 Knipscheer, A. Perrakis, V.A. Blomen, and T.R. Brummelkamp. 2017. Vasohibins encode
856 tubulin detyrosinating activity. *Science*. 358:1453-1456.
857 Nsamba, E.T., and M.L. Gupta. 2022. Tubulin isotypes - functional insights from model
858 organisms. *J Cell Sci*. 135.
859 O'Hagan, R., B.P. Piasecki, M. Silva, P. Phirke, K.C. Nguyen, D.H. Hall, P. Swoboda, and M.M.
860 Barr. 2011. The tubulin deglutamylase CCPP-1 regulates the function and stability of
861 sensory cilia in C. elegans. *Curr Biol*. 21:1685-1694.

862 Ori-McKenney, K.M., R.J. McKenney, H.H. Huang, T. Li, S. Meltzer, L.Y. Jan, R.D. Vale, A.P. Wiita,
863 and Y.N. Jan. 2016. Phosphorylation of beta-Tubulin by the Down Syndrome Kinase,
864 Minibrain/DYRK1a, Regulates Microtubule Dynamics and Dendrite Morphogenesis.
865 *Neuron*. 90:551-563.
866 Peris, L., M. Wagenbach, L. Lafanechere, J. Brocard, A.T. Moore, F. Kozielski, D. Job, L.
867 Wordeman, and A. Andrieux. 2009. Motor-dependent microtubule disassembly driven
868 by tubulin tyrosination. *J Cell Biol*. 185:1159-1166.
869 Portran, D., L. Schaedel, Z. Xu, M. Thery, and M.V. Nachury. 2017. Tubulin acetylation protects
870 long-lived microtubules against mechanical ageing. *Nat Cell Biol*. 19:391-398.
871 Puri, D., K. Ponniah, K. Biswas, A. Basu, S. Dey, E.A. Lundquist, and A. Ghosh-Roy. 2021. Wnt
872 signaling establishes the microtubule polarity in neurons through regulation of Kinesin-
873 13. *J Cell Biol*. 220.
874 Quintin, S., P.E. Mains, A. Zinke, and A.A. Hyman. 2003. The mbk-2 kinase is required for
875 inactivation of MEI-1/katanin in the one-cell Caenorhabditis elegans embryo. *EMBO*
876 *Rep*. 4:1175-1181.
877 Reed, N.A., D. Cai, T.L. Blasius, G.T. Jih, E. Meyhofer, J. Gaertig, and K.J. Verhey. 2006.
878 Microtubule acetylation promotes kinesin-1 binding and transport. *Curr Biol*. 16:2166-
879 2172.
880 Rogowski, K., J. van Dijk, M.M. Magiera, C. Bosc, J.C. Deloulme, A. Bosson, L. Peris, N.D. Gold, B.
881 Lacroix, M. Bosch Grau, N. Bec, C. Larroque, S. Desagher, M. Holzer, A. Andrieux, M.J.
882 Moutin, and C. Janke. 2010. A family of protein-deglutamylating enzymes associated
883 with neurodegeneration. *Cell*. 143:564-578.
884 Roll-Mecak, A. 2020. The Tubulin Code in Microtubule Dynamics and Information Encoding. *Dev*
885 *Cell*. 54:7-20.
886 Roth, D., B.P. Fitton, N.P. Chmel, N. Wasiluk, and A. Straube. 2018. Spatial positioning of EB
887 family proteins at microtubule tips involves distinct nucleotide-dependent binding
888 properties. *J Cell Sci*. 132.
889 Savage, C., M. Hamelin, J.G. Culotti, A. Coulson, D.G. Albertson, and M. Chalfie. 1989. mec-7 is a
890 beta-tubulin gene required for the production of 15-protofilament microtubules in
891 Caenorhabditis elegans. *Genes Dev*. 3:870-881.
892 Savage, C., Y. Xue, S. Mitani, D. Hall, R. Zakhary, and M. Chalfie. 1994. Mutations in the
893 Caenorhabditis elegans beta-tubulin gene mec-7: effects on microtubule assembly and
894 stability and on tubulin autoregulation. *J Cell Sci*. 107 (Pt 8):2165-2175.
895 Shida, T., J.G. Cueva, Z. Xu, M.B. Goodman, and M.V. Nachury. 2010. The major alpha-tubulin
896 K40 acetyltransferase alphaTAT1 promotes rapid ciliogenesis and efficient
897 mechanosensation. *Proc Natl Acad Sci U S A*. 107:21517-21522.
898 Sirajuddin, M., L.M. Rice, and R.D. Vale. 2014. Regulation of microtubule motors by tubulin
899 isotypes and post-translational modifications. *Nat Cell Biol*. 16:335-344.
900 Suryavanshi, S., B. Edde, L.A. Fox, S. Guerrero, R. Hard, T. Hennessey, A. Kabi, D. Malison, D.
901 Pennock, W.S. Sale, D. Wloga, and J. Gaertig. 2010. Tubulin glutamylation regulates
902 ciliary motility by altering inner dynein arm activity. *Curr Biol*. 20:435-440.
903 Taylor, S.R., G. Santpere, A. Weinreb, A. Barrett, M.B. Reilly, C. Xu, E. Varol, P. Oikonomou, L.
904 Glenwinkel, R. McWhirter, A. Poff, M. Basavaraju, I. Rafi, E. Yemini, S.J. Cook, A. Abrams,
905 B. Vidal, C. Cros, S. Tavazoie, N. Sestan, M. Hammarlund, O. Hobert, and D.M. Miller,

906 3rd. 2021. Molecular topography of an entire nervous system. *Cell*. 184:4329-4347
907 e4323.
908 Ti, S.C., M. Wieczorek, and T.M. Kapoor. 2020. Purification of Affinity Tag-free Recombinant
909 Tubulin from Insect Cells. *STAR Protoc*. 1.
910 Tischfield, M.A., G.Y. Cederquist, M.L. Gupta, Jr., and E.C. Engle. 2011. Phenotypic spectrum of
911 the tubulin-related disorders and functional implications of disease-causing mutations.
912 *Curr Opin Genet Dev*. 21:286-294.
913 Topalidou, I., C. Keller, N. Kalebic, K.C. Nguyen, H. Somhegyi, K.A. Politi, P. Heppenstall, D.H.
914 Hall, and M. Chalfie. 2012. Genetically separable functions of the MEC-17 tubulin
915 acetyltransferase affect microtubule organization. *Curr Biol*. 22:1057-1065.
916 van Dijk, J., K. Rogowski, J. Miro, B. Lacroix, B. Edde, and C. Janke. 2007. A targeted
917 multienzyme mechanism for selective microtubule polyglutamylation. *Mol Cell*. 26:437-
918 448.
919 Wang, S., N.H. Tang, P. Lara-Gonzalez, Z. Zhao, D.K. Cheerambathur, B. Prevo, A.D. Chisholm, A.
920 Desai, and K. Oegema. 2017. A toolkit for GFP-mediated tissue-specific protein
921 degradation in C. elegans. *Development*. 144:2694-2701.
922 Wolff, A., B. de Nechaud, D. Chillet, H. Mazarguil, E. Desbruyeres, S. Audebert, B. Edde, F. Gros,
923 and P. Denoulet. 1992. Distribution of glutamylated alpha and beta-tubulin in mouse
924 tissues using a specific monoclonal antibody, GT335. *Eur J Cell Biol*. 59:425-432.
925 Wu, Z., A. Ghosh-Roy, M.F. Yanik, J.Z. Zhang, Y. Jin, and A.D. Chisholm. 2007. Caenorhabditis
926 elegans neuronal regeneration is influenced by life stage, ephrin signaling, and synaptic
927 branching. *Proc Natl Acad Sci U S A*. 104:15132-15137.
928 Xia, L., B. Hai, Y. Gao, D. Burnette, R. Thazhath, J. Duan, M.H. Bre, N. Levilliers, M.A. Gorovsky,
929 and J. Gaertig. 2000. Polyglycylation of tubulin is essential and affects cell motility and
930 division in Tetrahymena thermophila. *J Cell Biol*. 149:1097-1106.
931 Xu, Z., L. Schaedel, D. Portran, A. Aguilar, J. Gaillard, M.P. Marinkovich, M. Thery, and M.V.
932 Nachury. 2017. Microtubules acquire resistance from mechanical breakage through
933 intralumenal acetylation. *Science*. 356:328-332.
934 Yan, C., F. Wang, Y. Peng, C.R. Williams, B. Jenkins, J. Wildonger, H.J. Kim, J.B. Perr, J.C.
935 Vaughan, M.E. Kern, M.R. Falvo, E.T. O'Brien, 3rd, R. Superfine, J.C. Tuthill, Y. Xiang, S.L.
936 Rogers, and J.Z. Parrish. 2018. Microtubule Acetylation Is Required for
937 Mechanosensation in Drosophila. *Cell Rep*. 25:1051-1065 e1056.
938 Yuan, Z., E.B. Becker, P. Merlo, T. Yamada, S. DiBacco, Y. Konishi, E.M. Schaefer, and A. Bonni.
939 2008. Activation of FOXO1 by Cdk1 in cycling cells and postmitotic neurons. *Science*.
940 319:1665-1668.
941 Zheng, C., M. Diaz-Cuadros, K.C.Q. Nguyen, D.H. Hall, and M. Chalfie. 2017. Distinct effects of
942 tubulin isotype mutations on neurite growth in Caenorhabditis elegans. *Mol Biol Cell*.
943 28:2786-2801.
944
945
946
947

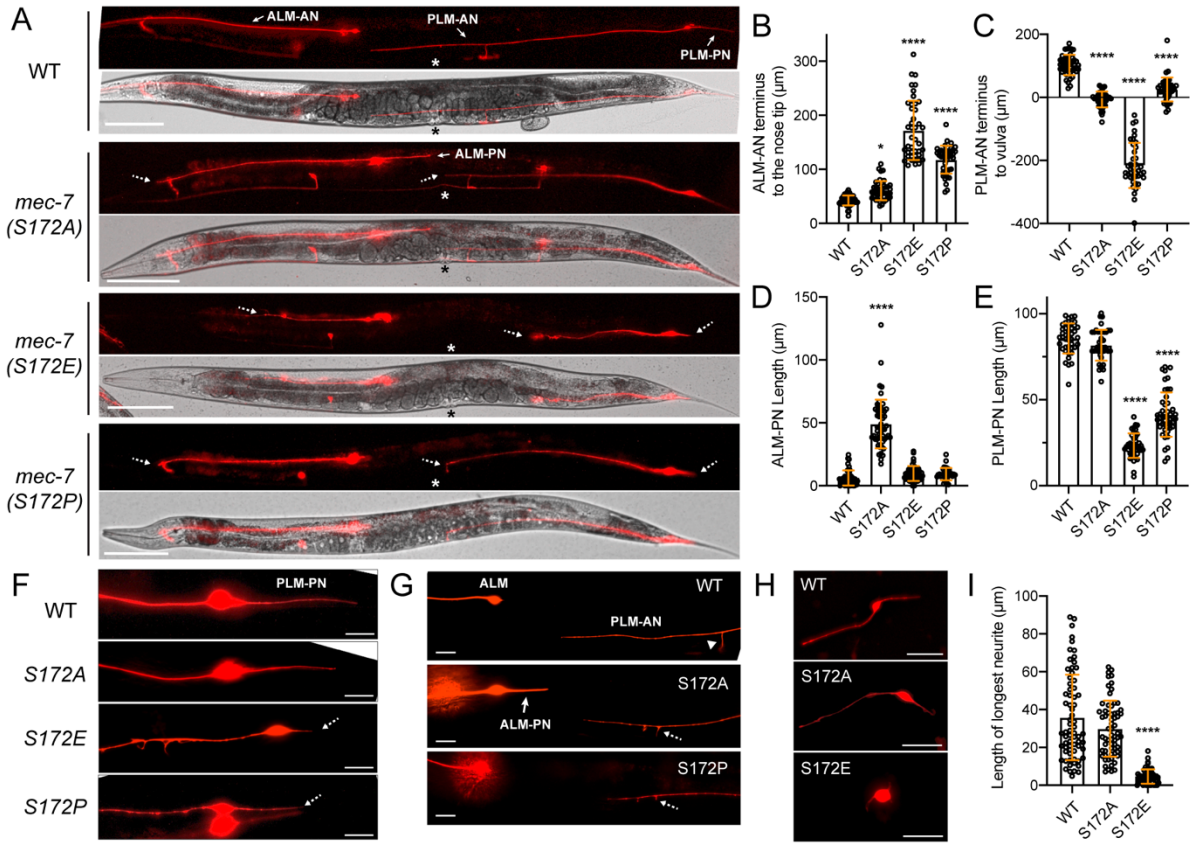

Figure 1. Substitution of MEC-7/β-tubulin S172 led to neurite growth defects in *C. elegans* TRNs. (A) TRN morphologies in wild-type animals, *S172A*, *S172E*, and *S172P* mutants. Specific neurites are labeled by arrows. Asterisks indicate the position of vulva. Dashed arrows point to the termini of neurites that are shortened in mutants. Scale bar = 100 µm. (B) The distance of ALM-AN terminus to the tip of the nose in various strains. The longer the distance, the shorter the ALM-AN. One and four asterisks indicate $p < 0.05$ and 0.0001, respectively, in statistical significance when compared with the wild type. (C) The distance from the PLM-AN terminus to the vulva in various strains. If the anteriorly directed PLM-AN grew past the vulva, the distance is positive. If PLM-AN cannot reach the vulva, the distance is negative. (D) Quantification of ALM-PN length. The wild-type animals have no or very short ALM-PN. (E) Quantification of PLM-PN length. (F) Representative images of PLM-PN in various strains. Dashed arrows indicate the neurite termini of shortened PLM-PN. (G) Representative images of ALM-PN in *mec-7(S172A)* mutants. Arrowhead indicates the synaptic branch of PLM-AN in the wild-type animals. Dashed arrows point to the branching defects where the synaptic branch failed to extend to the ventral cord. (H) TRNs extracted from the embryos of S172 mutants and cultured *in vitro*; they were identified by their expression of *mec-17p::TagRFP* among the embryonic cells. TRNs from *S172E* mutants had no or very short neurites. (I) The length of the longest neurite of the *in vitro* cultured TRNs from the S172 mutants. Scale bar = 20 µm.

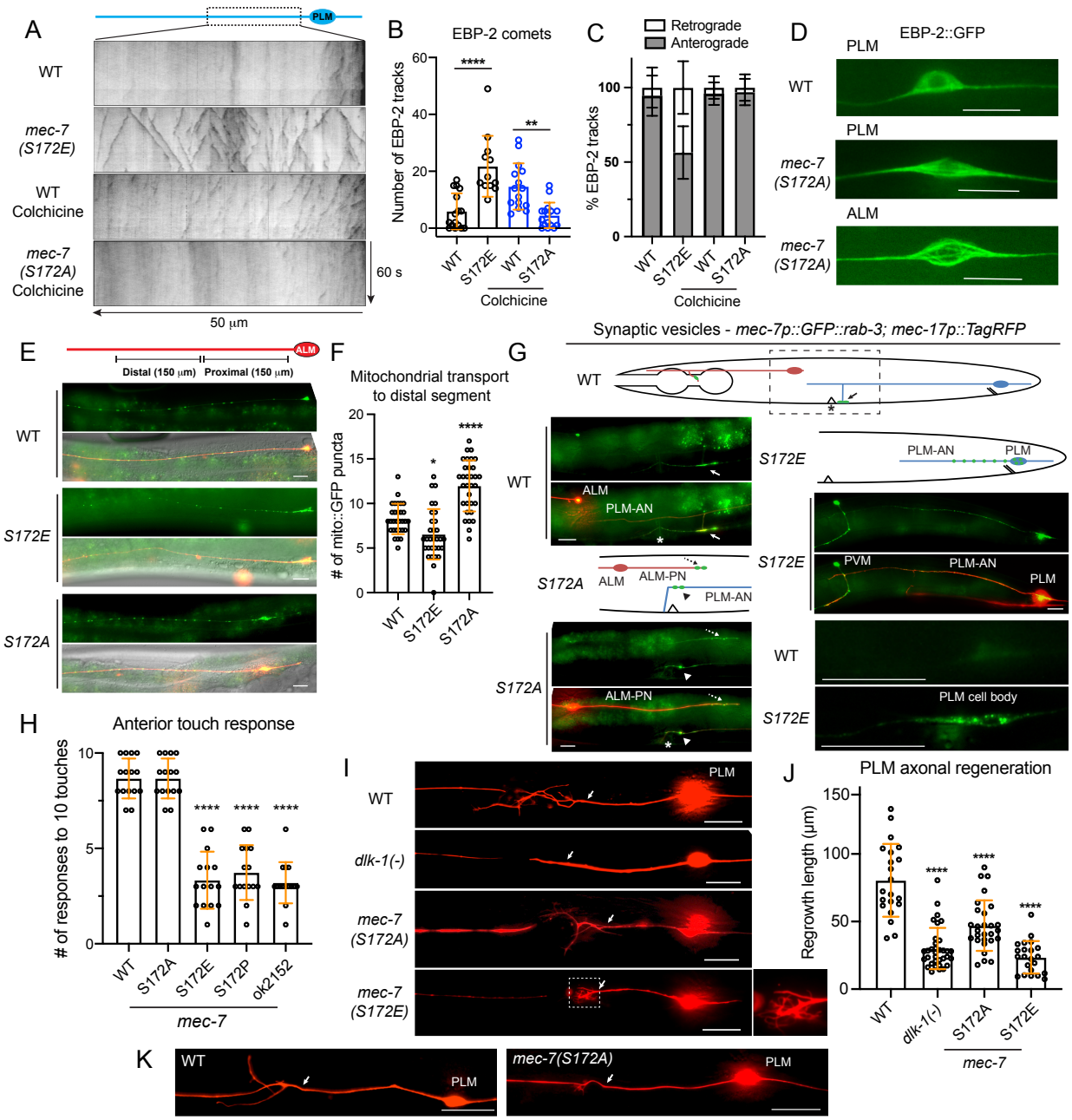

Figure 2. MEC-7/β-tubulin S172 phosphorylation regulates MT dynamics, cargo transport, mechanosensory function, and axonal regeneration. (A) Representative kymographs of EBP-2::GFP dynamics in the PLM-AN of various strains. The wild-type animals and *S172A* mutants were subjected to a mild colchicine treatment to increase MT dynamics and imaged after one-hour recovery. (B) Quantification of the number of EBP-2 tracks. One, two, and four asterisks indicate $p < 0.05$, 0.01, and 0.0001, respectively, in statistical significance when compared with the wild type. (C) Percentages of retrograde and anterograde movement for the EBP-2 comets. (D) Comparison of the EBP-2::GFP signal in the cell body of wild-type and *mec-7(S172A)* animals. (E) Distribution of mitochondria in the ALM-AN indicated by the *jsIs609 [mec-7p::mitoGFP]* signal. (F) The quantification of the number of mitoGFP puncta in the distal segment of ALM-AN (150-300 µm away from the cell body). (G) Localization of the synaptic

vesicles (GFP::RAB-3), which are indicated by green dots in the cartoon in S172 mutants. The fluorescent image for the wild type is a representative image of the region in the dashed box of the cartoon; arrows indicate the normal localization of RAB-3 signal to the synapses made by synaptic branch of PLM-AN in the ventral nerve cord posterior to the vulval position (indicated by the asterisk). In S172A mutants, RAB-3 is mistargeted to the ALM-PN (dashed arrow) and accumulates at the PLM-AN (arrowhead) when the synaptic branch fails to extend, and the axon hooks ventrally. In S172E mutants, RAB-3 signal was trapped in the cell body as PLM-AN is severely shortened. (H) Anterior touch responses of various *mec-7* mutants; *mec-7(ok2151)* is a deletion allele. (I) Representative axonal regrowth of PLM-AN following laser axotomy in various strains; arrows indicate the cut site. (J) Quantification of PLM regrowth length for the regrowth cases. (K) Examples of reconnections after laser axotomy; arrows indicate the cut site. Scale bars = 20 μm for all panels.

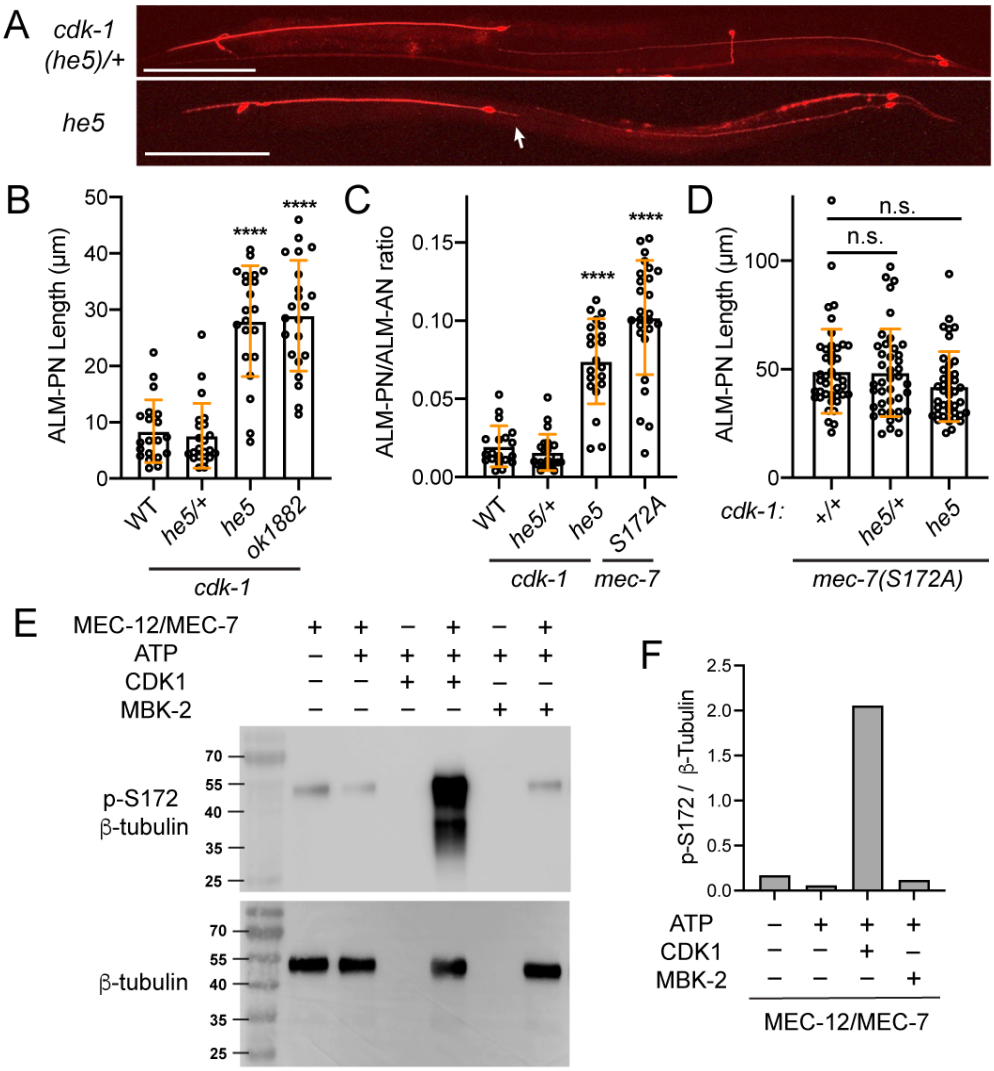

Figure 3. CDK-1 mediates MEC-7/β-tubulin S172 phosphorylation and regulates neurite growth. (A) Images of TRN morphologies in *cdk-1(he5)/+* heterozygotes and *cdk-1(he5)* homozygotes (escapers). Arrow points to the ectopic ALM-PN. Scale bar = 100 μm. (B) The length of ALM-PN in wild-type and *cdk-1* mutants. ALM-PN length in the escapers of *he-5* and *ok1882* homozygous mutants were measured. (C) The ratio of ALM-PN length to ALM-AN length in various strains. (D) The ALM-PN length in animals carrying both *mec-7(S172A)* and *cdk-1* mutations. (E) Western blot of the kinase reaction samples using anti-phospho-S172 (p-S172) antibodies. The kinase reaction was conducted in the MEM buffer with 475 nM CDK1/Cyclin B or 500 nM MBK-2m. The weak p-S172 signal in the first lane likely resulted from the nonspecific interaction of the anti-p-S172 antibodies with the unmodified MEC-12/MEC-7 heterodimer or the background phosphorylation level of the recombinant dimer. Anti-β-tubulin antibodies were used to ensure the equal loading of the tubulin dimers. (F) Quantification of the grey intensity ratio of p-S172 to β-tubulin signals in the western blot.

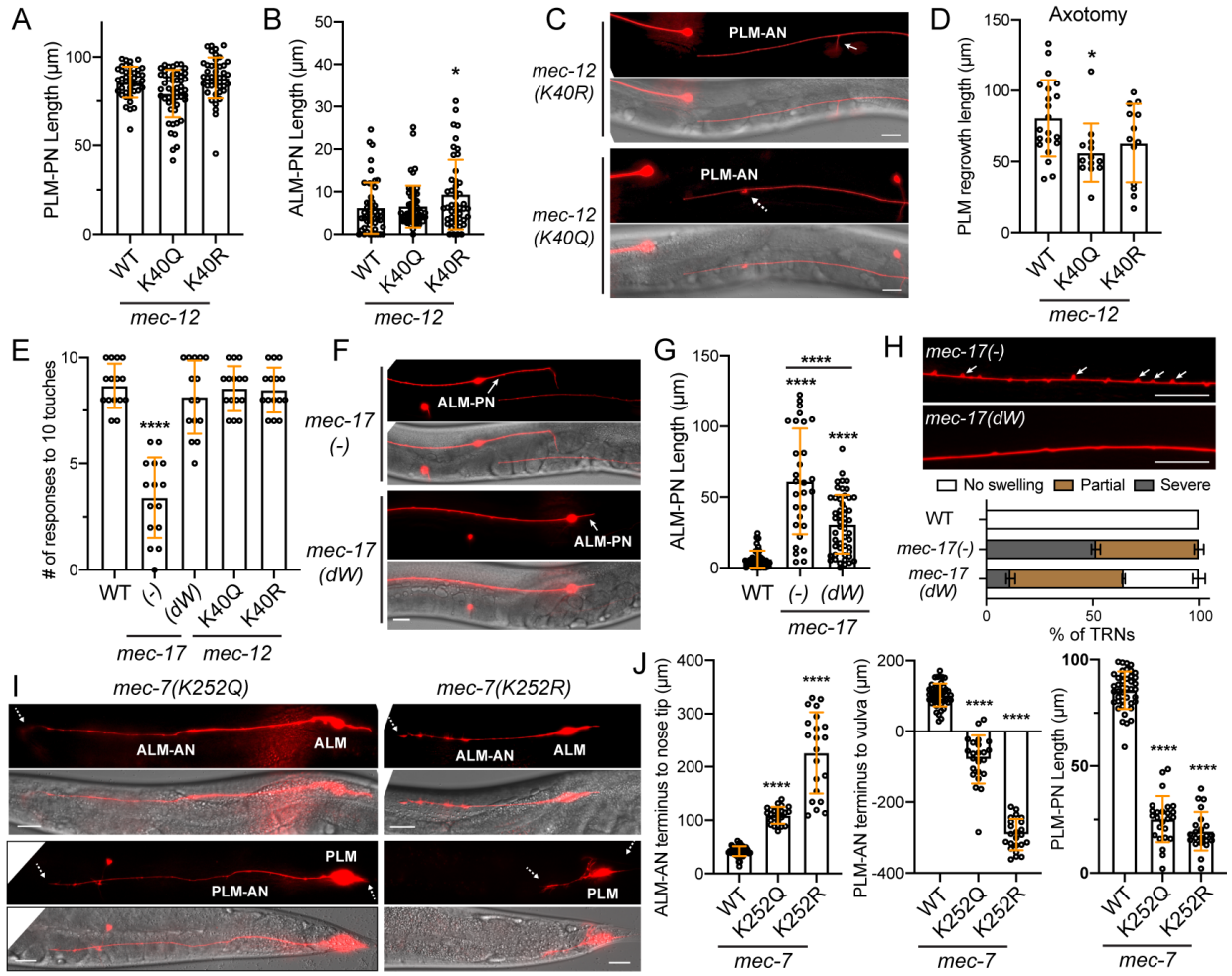

Figure 4. The effects of tubulin acetylation on neurite development. (A) The PLM-PN length in *mec-12* K40 mutants. (B) The length of ALM-PN in *mec-12* K40 mutants. (C) 20% of PLM-AN failed to extend the synaptic branch in *mec-12(K40Q)* mutants. Arrow points to the normal synaptic branch in *mec-12(K40R)* mutants and the dashed arrow indicates the branching defects. See Figure 1G for the wild-type control. (D) Quantification of the PLM regrowth length after laser axotomy in *mec-12* K40 mutants. (E) Anterior touch responses of *mec-17* and *mec-12* mutants. The deletion allele *ok2109* was used for *mec-17(-)* and the *unk126* (G121W & G123W) allele was used for *mec-17(dW)*. (F) Comparison of ALM-PN in *mec-17(-)* and *mec-17(dW)* mutants. (G) Quantification of ALM-PN lengths in *mec-17* mutants. Four asterisks indicate $p <$ 0.0001 in a post-ANOVA Tukey's honestly significant difference (HSD) test. (H) Comparison and quantification of the neurite swelling and looping phenotypes in *mec-17(-)* and *mec-17(dW)* mutants (ALM-AN is shown). For the quantification, severe swelling is defined by having two or more bumps taller than 1 µm within 100 µm length of axon; partial swelling is defined by having smaller or fewer bumps than the severe ones; no swelling is defined by having no > 0.5 µm bumps in the entire axon. (I) The ALM and PLM morphologies in *mec-7* K252 mutants. Dashed arrows point to the termini of the shortened ALM-AN or PLM-AN or PLM-PN. See Figure 1A for the wild-type control. (J) Quantification of the shortening of the three neurites. For ALM-AN, the distance from the neurite ending to the nose tip was measured; the bigger the gap, the

shorter the ALM-AN. For PLM-AN, the distance from the neurite terminus to the vulva was measured. Positive value means the neurite grew past the vulva and negative value means the neurite did not reach the vulva. Scale bars = 20 μm for all panels.

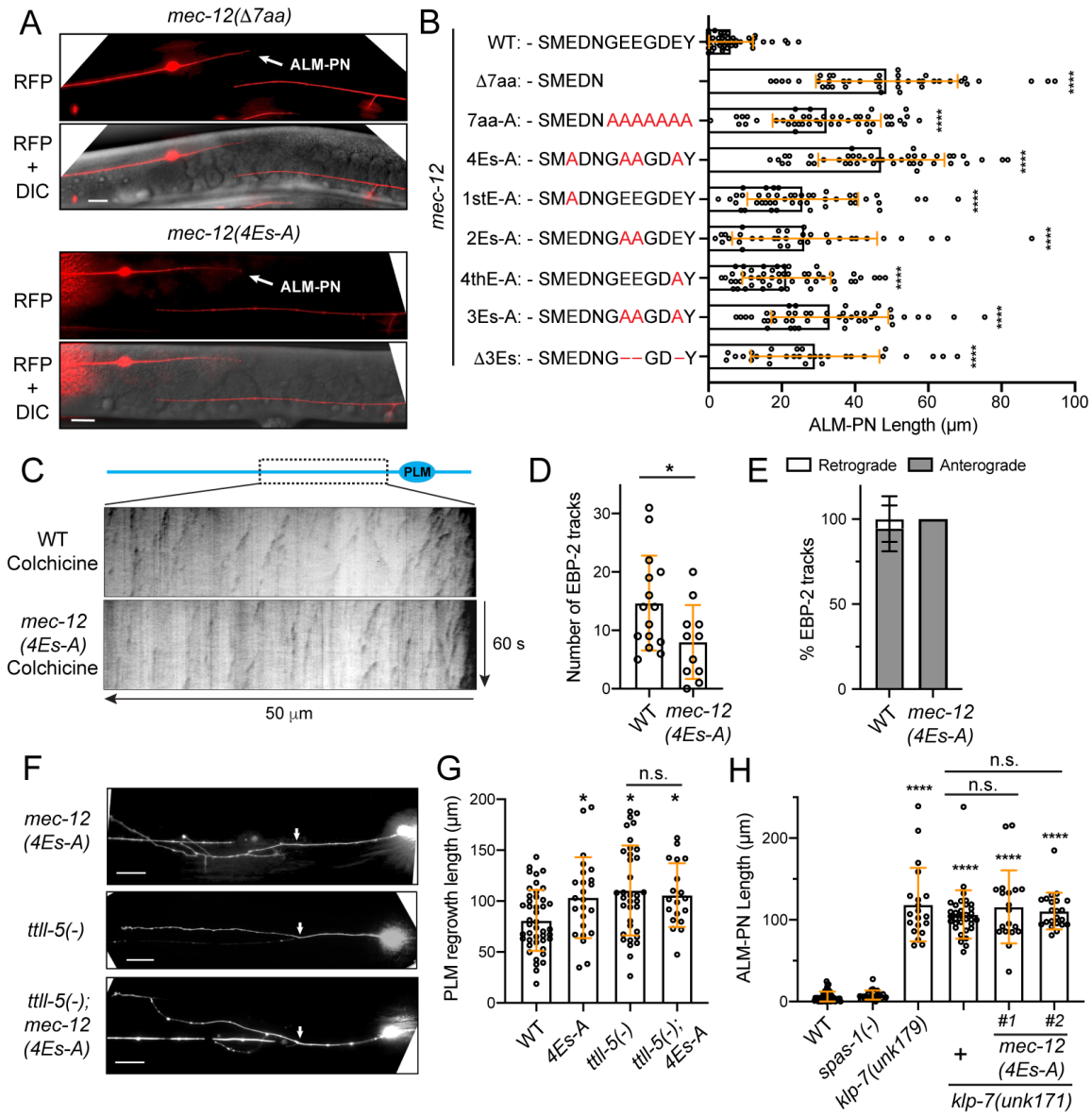

Figure 5. Tubulin polyglutamylation regulates neurite growth and regeneration. (A) The growth of ectopic ALM-PN (arrow) in *mec-12* mutants lacking the polyglutamylation sites. (B) The quantification of ALM-PN length in various *mec-12* mutant strains. The changes made to the last twelve amino acids of MEC-12 in the various alleles are shown. (C) Kymographs showing EBP-2::GFP dynamics in wild-type and *mec-12(4Es-A)* animals after a mild colchicine treatment and a one-hour recovery. (D) Quantification of the number of EBP-2 comets in *mec-12(4Es-A)* mutants. (E) The percentage of retrograde and anterograde EBP-2 movements. (F) PLM regrowth following laser axotomy in *mec-12(4Es-A)* and *ttll-5(tm3360)* mutants and the double mutants; arrows indicate the cut site. (G) The quantification of PLM regrowth length in various strains. (H) ALM-PN lengths in *spas-1(tm683)*, *klp-7(unk179; Δ11bp)*, *klp-7(unk171; Δ14bp)*, and *klp-7; mec-12(4Es-A)* double mutants. *unk171* was generated by gene editing in both the wild-type and the *mec-12(4Es-A)* background, and #1 and #2 were two independent lines. See Figure 5-figure supplement 2 for the details of the *klp-7* alleles. Scale bars = 20 μm for all panels; n.s. indicates no statistical significance in a post-ANOVA Tukey's HSD test.

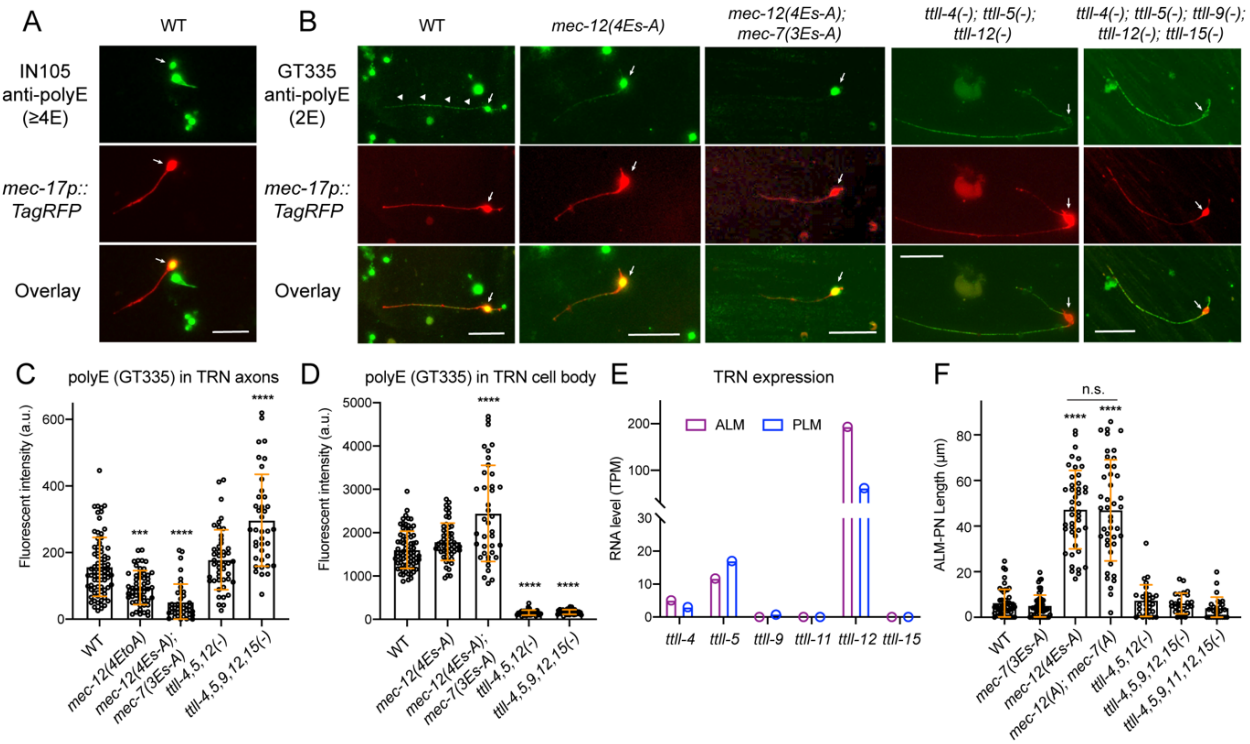

Figure 6. Substitution of glutamates in MEC-12 and MEC-7 C-terminal tails eliminate tubulin polyglutamylation in the axons. (A) Antibody staining of *in vitro* cultured TRNs (labeled by RFP) with IN105 anti-polyglutamylation antibodies that recognize a chain of four or more glutamates. (B) Antibody staining of *in vitro* cultured TRNs from various strains with GT335 anti-polyglutamylation antibodies that recognize the branchpoint and a side chain of two glutamyl units. CGZ1554 *ttll-4(tm3310); ttll-5(tm3360); ttll-12(unk185); uIs115* and CGZ1475 *ttll-4(tm3310); ttll-5(tm3360) ttll-9(tm3889) ttll-15 (tm3871); ttll-12(unk185); uIs115* were used in the experiment. Arrows point to the TRN cell bodies and arrowheads point to the staining signal in the axon. (C-D) Quantification of the fluorescent intensity (in arbitrary units or a.u.) for the polyE staining of TRN axons and cell bodies using GT335. (E) RNA level of the *ttll* genes in ALM and PLM neurons according to the L4 stage single-cell transcriptomic data obtained from wormbase.org. (F) ALM-PN length in *mec-7*, *mec-12*, and *ttll* mutant strains. CGZ1554, CGZ1475, and CGZ1474 *ttll-4(tm3310); ttll-11(tm4059); ttll-5(tm3360) ttll-9(tm3889) ttll-15(tm3871); ttll-12(unk185); zdIs5* were used. Scale bars = 20 μm for all panels. Three and four asterisks indicate $p < 0.001$ and 0.0001, respectively, in a post-ANOVA Dunnett's test comparing all mutants with the wild-type animals.

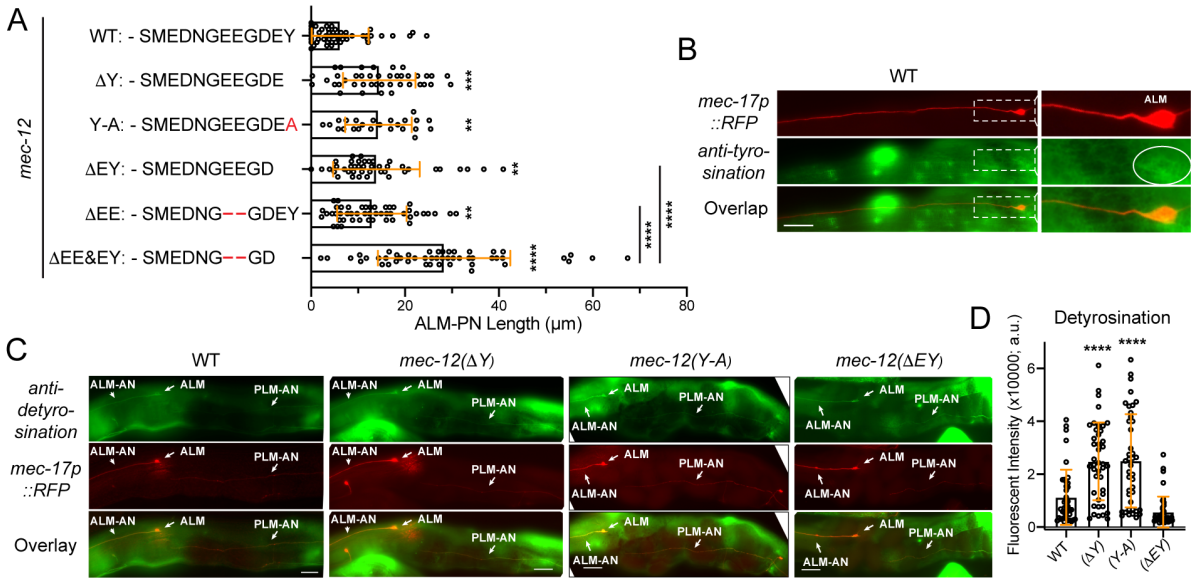

Figure 7. The effects of tubulin detyrosination and Δ2 modification on neurite growth. (A) The length of ALM-PN in strains deleting the terminal tyrosine or the last two residues. Two, three, and four asterisks correspond to $p < 0.05$, 0.001, and 0.0001, respectively, in a post-ANOVA Tukey's HSD test. (B) The weak staining of wild-type TRNs with the anti-tyrosinated α-tubulin antibodies. (C) The staining of the wild-type animals and the various *mec-12* mutants with anti-detyrosinated α-tubulin antibodies. Arrows point to the ALM cell bodies, ALM-AN, and PLM-AN (zoom in to see the signal). (D) Quantification of the fluorescent intensity of the anti-detyrosination staining signal in the axons. Arbitrary units (a.u.) were used.

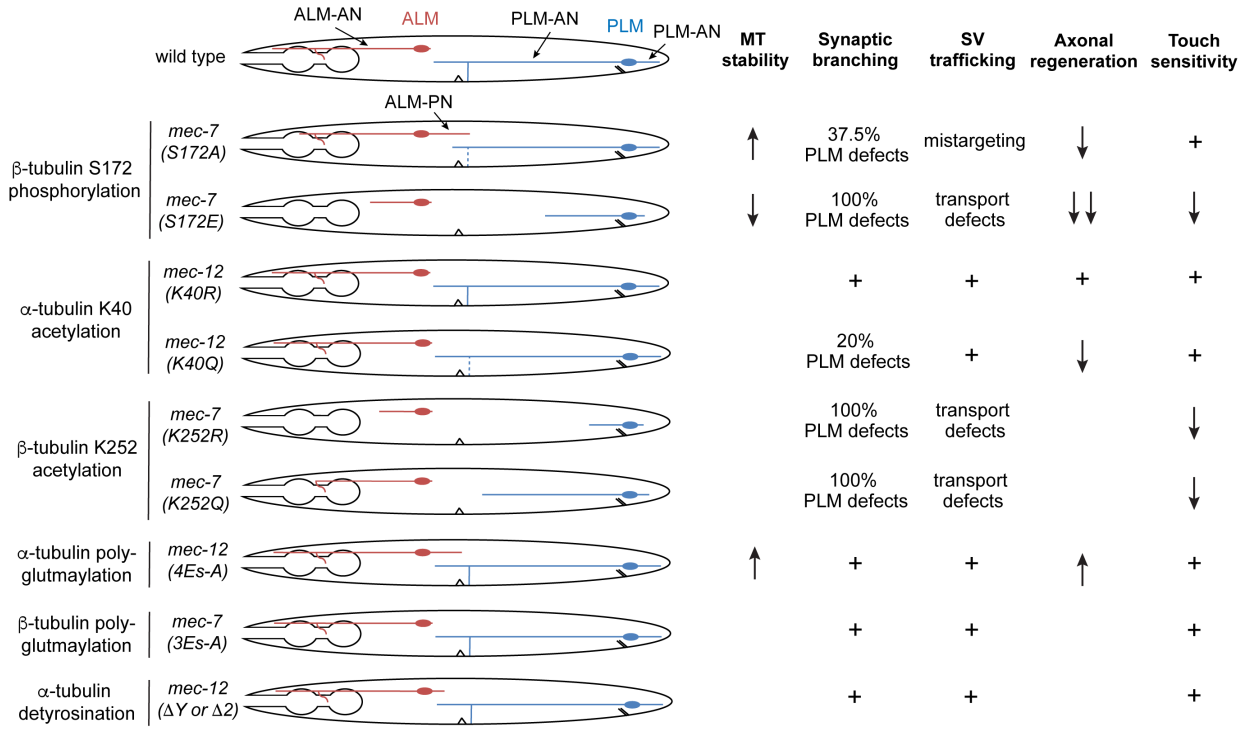

Figure 8. Summary of the phenotypes of the tubulin PTM site mutants. Cartoons represent the morphologies of the ALM and PLM neurons in various *mec-7* and *mec-12* mutants. Severe shortening of neurites often represents phenotypes of antimorphic alleles, while the growth of a prominent ALM-PN is characteristic of neomorphic alleles. Dashed lines indicated partial defects of forming the PLM synaptic branch. For synaptic vesicle (SV) trafficking, mistargeting means SV is trafficked to ALM-PN; transport defects mean that SV is mostly trapped in cell bodies or proximal segment of the neurite. MT stability is measured by EBP-2 comets; increased EBP-2 dynamics indicates reduced MT stability, and reduced EBP-2 dynamics indicates elevated MT stability. Blank space means phenotype not determined; + means phenotype similar to the wild-type animals.

1133 **Figure Supplements**

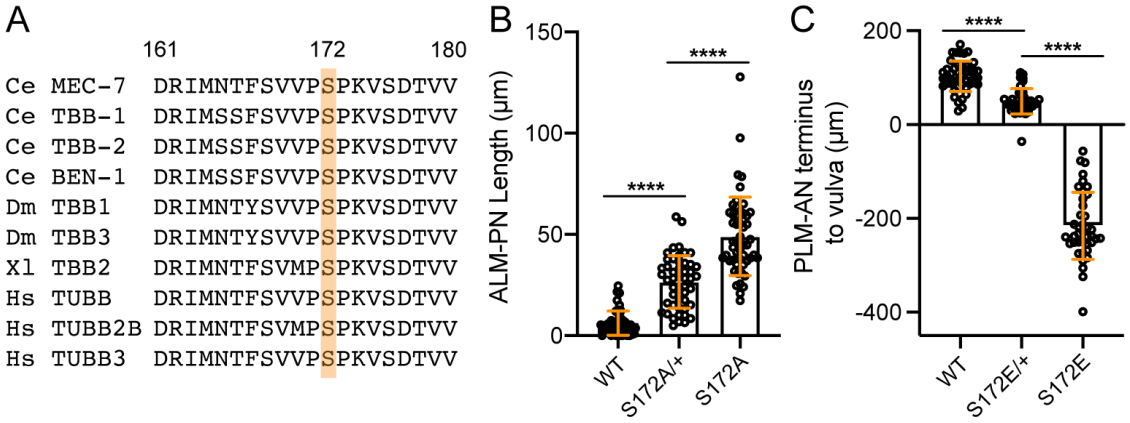

1134
1135 **Figure 1-figure supplement 1. *mec-7* S172A and S172E mutations are semidominant.** (A)
1136 Evolutionary conservation of S172 (highlighted) and flanking sequences among β-tubulin genes
1137 across species. Ce for *C. elegans*, Dm for *Drosophila melanogaster*, Xl for *Xenopus laevis*, and
1138 Hs for *Homo sapiens*. (B) The length of ALM-PN in day-one adults (three days after bleaching)
1139 of wild-type animals, *mec-7(S172A)/+* heterozygotes, and *mec-7(S172A)* homozygotes. (C) The
1140 distance from the PLM-AN terminus to the vulva in the wild-type animals, *mec-7(S172E)/+*
1141 heterozygotes, and *mec-7(S172E)* homozygotes. If PLM-AN grew past the vulva, the distance is
1142 positive. If PLM-AN cannot reach the vulva, the distance is negative. Four asterisks indicate $p <$
1143 0.0001 in a post-ANOVA Tukey's HSD test.
1144
1145
1146
1147
1148
1149
1150
1151
1152
1153
1154

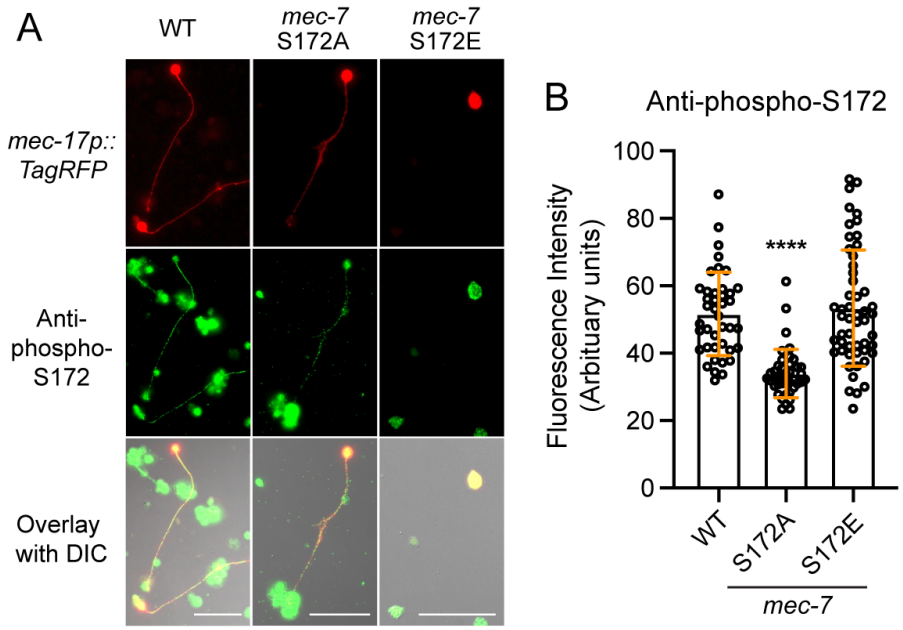

Figure 1-figure supplement 2. *mec-7* S172 mutations altered β-tubulin S172 phosphorylation level. (A) Anti-β-tubulin phospho-S172 antibody staining of *in vitro* cultured *C. elegans* embryonic cells from the indicated strains. Cells expressing the *mec-17p::TagRFP* were identified as the TRNs. Scale bar = 20 μm. (B) Fluorescent intensity in the axons were measured and quantified. Four asterisks indicate $p < 0.0001$ in a Dunnett's test comparing the mutant cells with the wild-type cells.

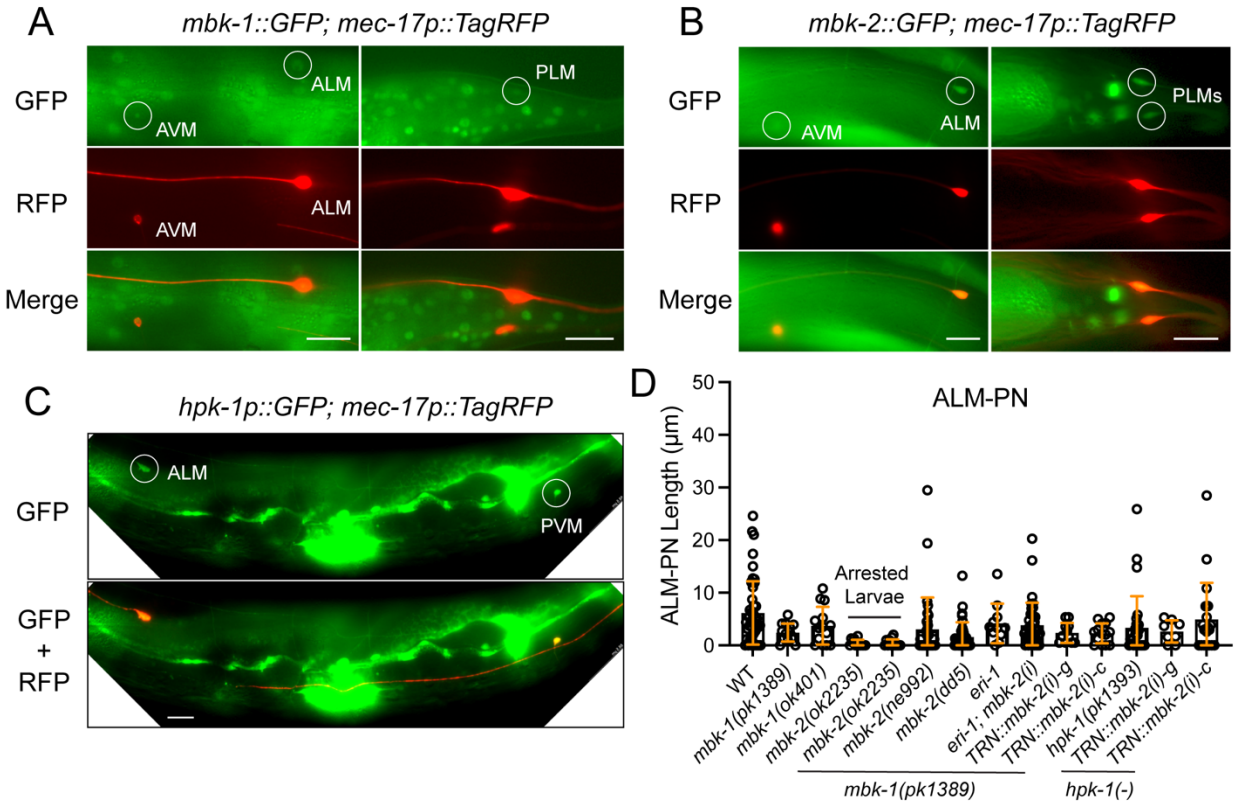

Figure 3-figure supplement 1. Expression and phenotypes of the minibrain homologs, *mbk-1*, *mbk-2*, and *hpk-1* in the TRNs. (A) The expression of *cmIs6 [mbk-1::GFP]* in the TRNs labeled by *mec-17p::TagRFP*. Circles indicate the expression of GFP in TRNs, including ALM, PLM, and AVM neurons. (B) The expression of *cmEx6 [mbk-2p::GFP]* in the TRNs. (C) The expression of *unkEx194 [hpk-1Bp::GFP]* in TRNs. Scale bar = 20 μm for all panels. (D) Quantifications of ALM-PN length in various strains. ALM-PN was measured in the arrested larvae of the *mbk-2(ok2235)* single and *mbk-1(pk1389); mbk-2(ok2235)* double mutants; the rest were measured in adults. Both *ne992* and *dd5* are temperature-sensitive alleles and were first grown at 15 °C to L1 stage and then shifted to 25 °C and scored at adult stage. *mbk-2(i)* indicates feeding RNAi done in the CGZ963 *mbk-1(pk1389) X; eri-1(mg366ts) IV; uIs115 IV* strain for enhanced RNAi. *TRN::mbk-2(i)-g* and *-c* indicate double strand RNA expressed from the TRN-specific *mec-17* promoter against the genomic DNA and cDNA of *mbk-2*, respectively.

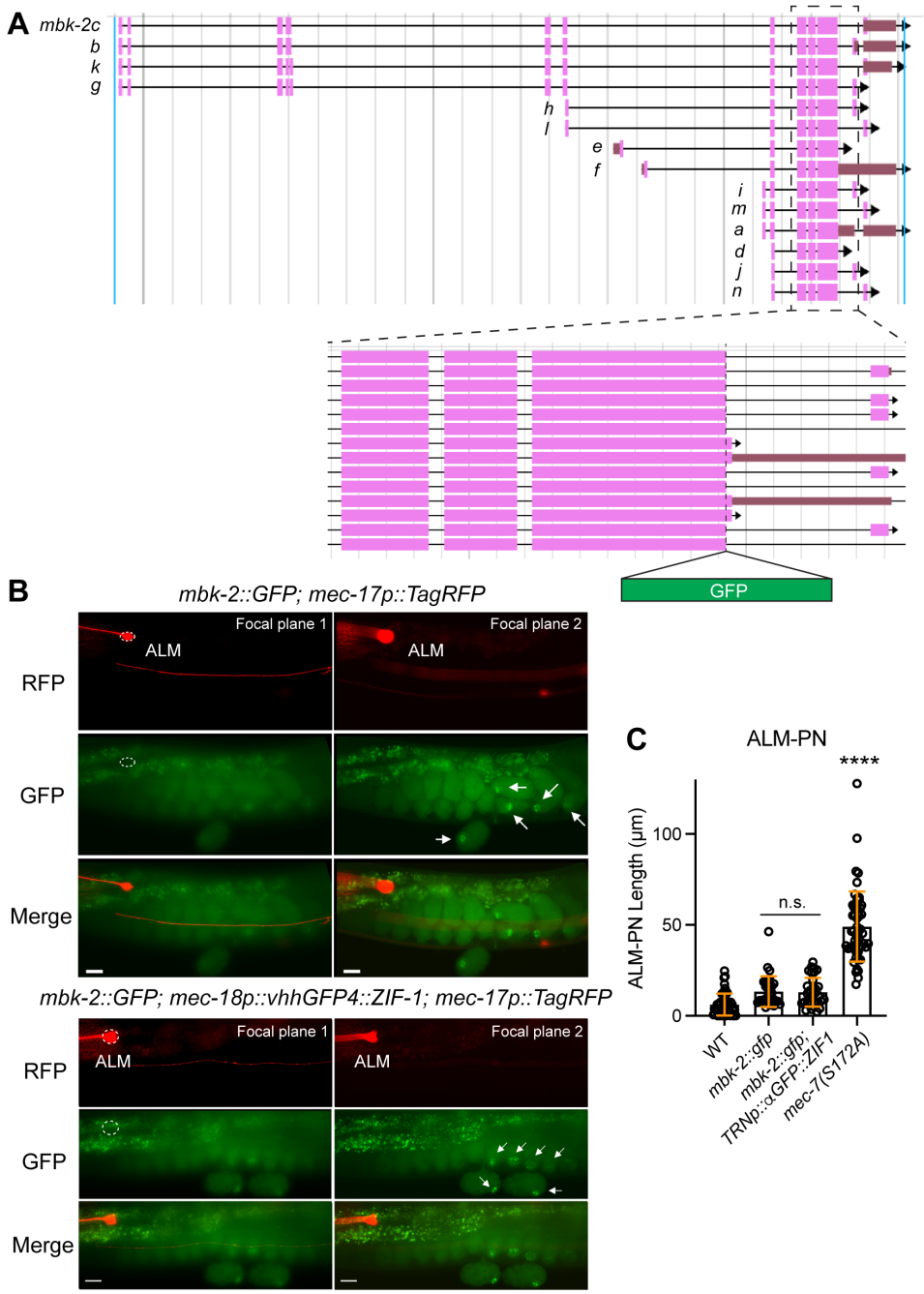

Figure 3-figure supplement 2. Potential TRN-specific degradation of MBK-2 does not result in the growth of long ALM-PN. (A) Gene structure of *mbk-2* downloaded from Wormbase.org (WS292); the exon structures of 14 isoforms are shown. Dashed box is enlarged to show the GFP insertion site. (B) Expression of MBK-2::GFP in adult animals with or without the TRN-specific expression of ZIF-1 fused with anti-GFP nanobodies (*vhhGFP4::ZIF-1*). No GFP signals (dashed circles) were detected in TRNs labeled by *mec-17p::TagRFP*, but GFP signals (arrows) were found in the embryos (with potential concentration in the P lineage). (C) Quantification of ALM-PN length in various strains. n.s. indicates no statistical significance in a post-ANOVA Tukey's HSD test. Four asterisks indicate $p < 0.0001$ in comparison with the wild-type animals.

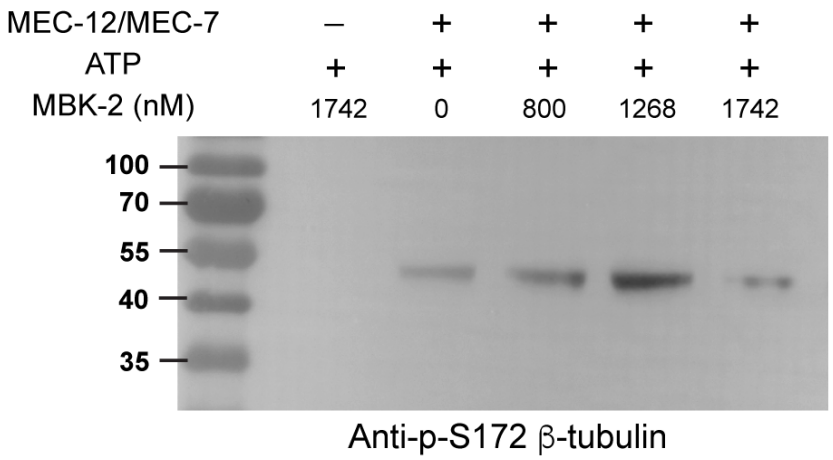

Figure 3-figure supplement 3. Kinase assay for MBK-2 in BRB80 buffer. 500 nM recombinant MEC-12/MEC-7 heterodimer and 1 mM ATP were incubated with various concentration of MBK-2. Western blot of the kinase reaction samples was done using the anti-phospho-S172 antibodies.

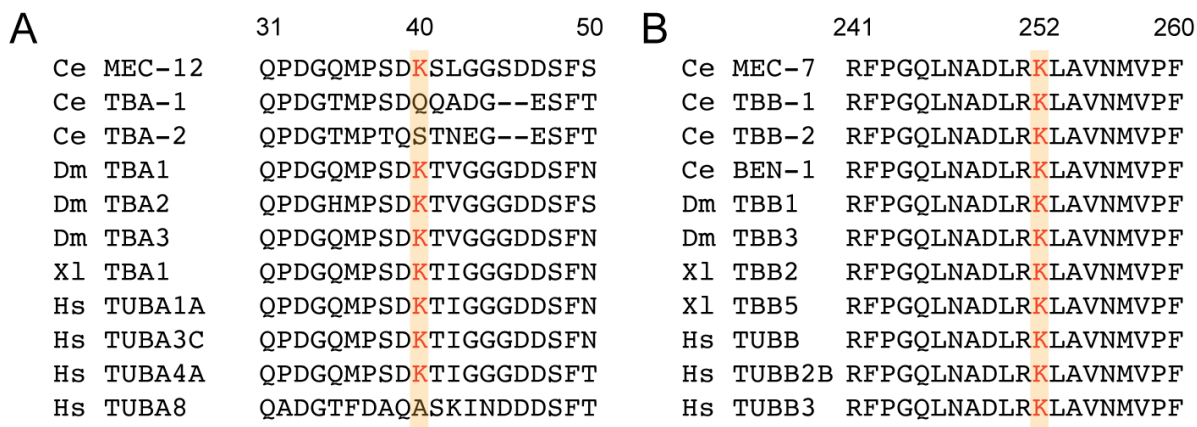

Figure 4-figure supplement 1. Evolutionary conservation of α-tubulin K40 and β-tubulin K252 residues. (A) Comparison of K40 (highlighted) and the flanking sequences (a.a. 31-40) in MEC-12 with other α-tubulin genes across species. Ce for *C. elegans*, Dm for *Drosophila melanogaster*, Xl for *Xenopus laevis*, and Hs for *Homo sapiens*. (B) The conservation of K252 (highlighted) and the adjacent sequences (a.a. 241-260) among β-tubulin genes across species.

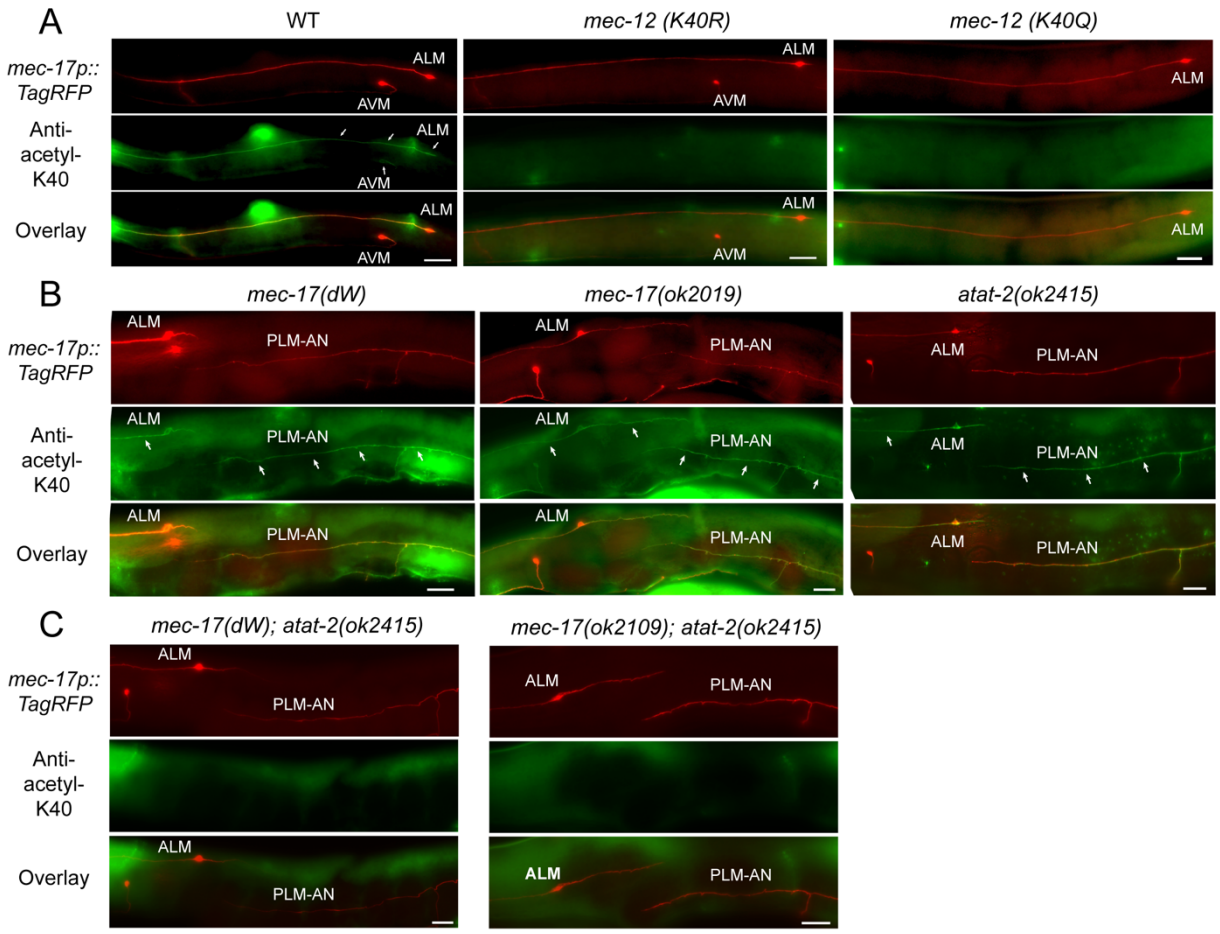

Figure 4-figure supplement 2. *mec-12* K40R and K40Q mutations and the combined loss of *mec-17* and *atat-2* affect α-tubulin K40 acetylation. (A) Anti-acetyl-K40 staining of the wild-type, *mec-12(K40R)*, and *mec-12(K40Q)* animals. Only the wild-type animals showed the staining in TRNs. Neither *mec-12(K40R)* nor *mec-12(K40Q)* mutants showed any staining. Arrows point to the staining signal in cell bodies or axons. Scale bar = 20 μm. (B-C) Anti-acetyl-K40 staining of acetyltransferase mutants. *mec-17(dW)*, *mec-17(-)*, and *atat-2(-)* single mutants showed clear staining signal, whereas the *mec-17; atat-2* double mutants showed no signal at all. Arrows point to the staining signal in the neurites. Scale bar = 20 μm.

```
TBA-8   EGEFMEARDDLAALEKDYAEVSRDTADLEEENDEF---------:452
TBA-6   EGEFSEAREDMAALEKDYEEIGEDELPDDIDDQSYRGRSSGSRY:464
TBA-5   EGEFSEAREDMAALEKDYEEVGVDSFDPNDEEY-----------:447
TBA-9   EGEFSEAREDLAALEKDYEEVGLDAGEPDEEDD-------YSHY:456
TBA-7   EGEFSEAREDLAALEKDYEEVGADSDANDNG---------DDEY:444
MEC-12  EGEFSEAREDLAALEKDYEEVGVDSMEDNG-EE-------GDEY:450
TBA-4   EGEFTEAREDLAALEKDYEEVGADSNEGL-EED-------GEEY:448
TBA-1   EGEFTEAREDLAALEKDYEEVGADSNEGGNEEE-------GEEY:454
TBA-2   EGEFTEAREDLAALEKDYEEVGADSNEGGEE-E-------GEEY:448
        **** ***:*:******* *:. *
```

Figure 5-figure supplement 1. Sequence divergence of α-tubulin C-terminal tails in *C. elegans*. Comparison of the amino acid sequences of the C-terminal region of the α-tubulin isotypes. The last twelve amino acids of MEC-12 are highly divergent among the isotypes (boxed region).

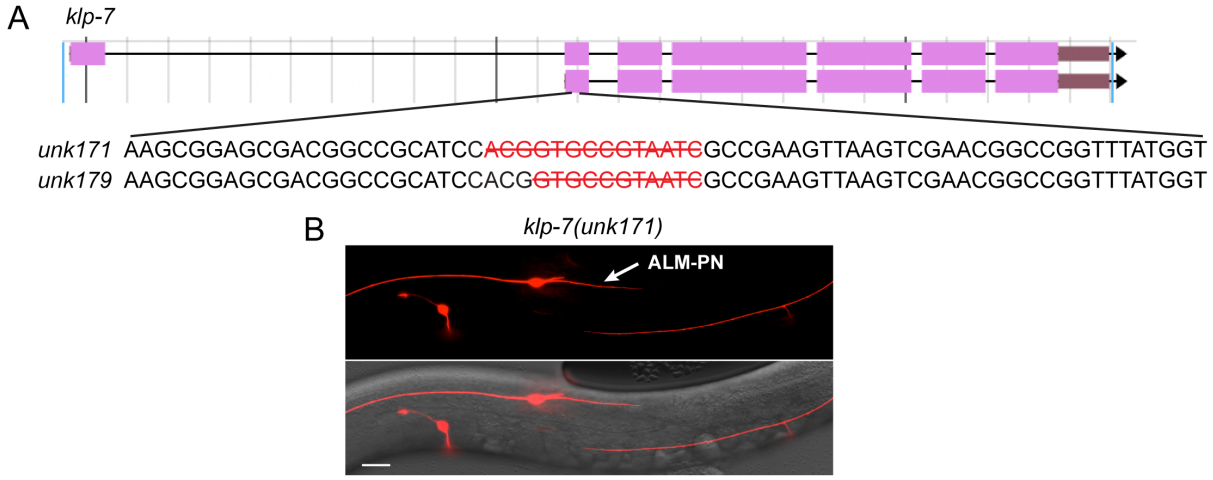

Figure 5-figure supplement 2. Mutations in *klp-7* result in the growth of an ectopic ALM-PN. (A) The gene structure of *klp-7* (from Wormbase.org) and the nucleotides deleted in *unk171* and *unk179* alleles, which were generated by CRISPR/Cas9-mediated gene editing. (B) The ectopic ALM-PN in *klp-7(unk171)* mutants.

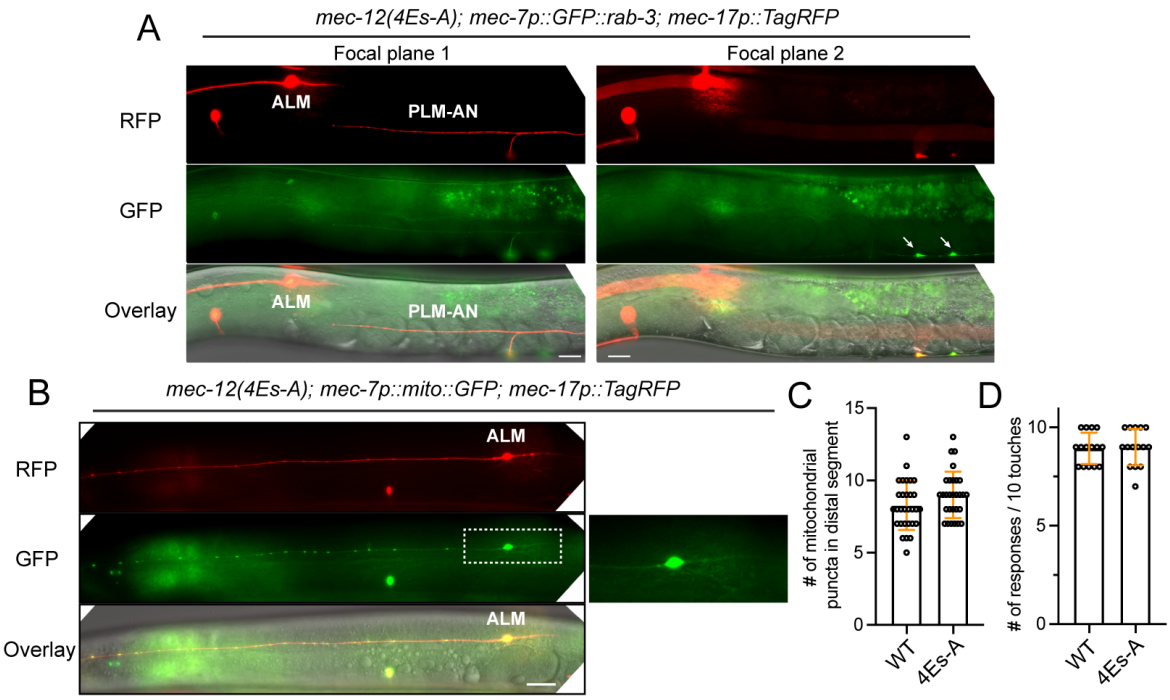

Figure 5-figure supplement 3. The lack of cargo transport and mechanosensory defects in *mec-12(4Es-A)* mutants. (A) The normal localization of synaptic vesicles (GFP::RAB-3) to the synaptic branch (arrows) of PLM-AN in *mec-12(4Es-A)* mutants. Focal plane 1 focuses on the neurites, while focal plane 2 focuses on the ventral cord. (B) Distribution of mitochondria in the ALM-AN of *mec-12(4Es-A)* mutants. (C) Quantification of the number of mito::GFP puncta in the distal segment (150~300 μm from the cell body) of ALM-AN. (D) Anterior touch response in the *mec-12(4Es-A)* mutants.

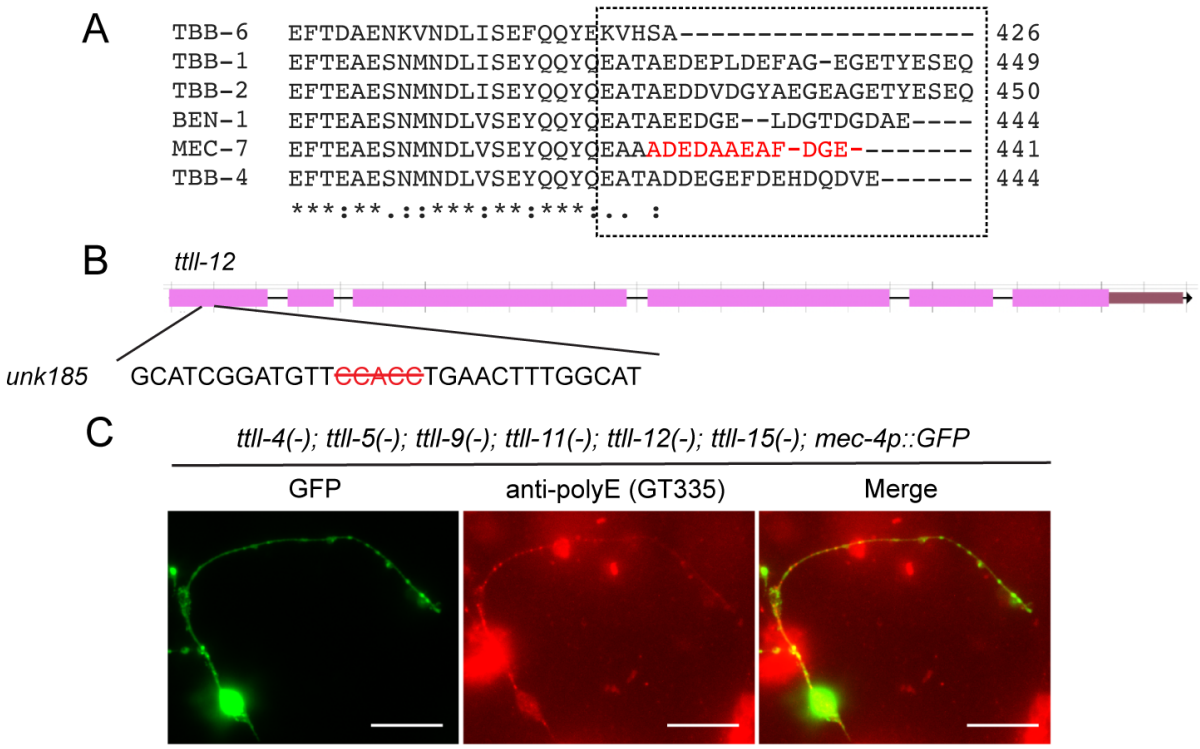

Figure 6-figure supplement 1. Sequence divergence of the C-terminal tail among β-tubulin isotypes and the molecular details of *ttll-12* CRISPR allele. (A) Comparison of the amino acid sequences of the C-terminal region of the β-tubulin isotypes in *C. elegans*. The last twelve amino acids of MEC-7 are divergent among the isotypes (boxed region). (B) Five nucleotides (red with strikethrough) were deleted in *ttll-12(unk185)* allele. (C) Anti-polyglutamylation staining of CGZ1474 *ttll-4(tm3310) III; ttll-11(tm4059) IV; ttll-5(tm3360) ttll-9(tm3889) ttll-15(tm3871) V; ttll-12(unk185) II; zdIs5[mec-4p::GFP] I* with GT335 antibodies and rhodamine-conjugated rabbit anti-mouse secondary antibodies. The staining pattern is similar to the quintuple mutants shown in Figure 6B.